

Tornado Detection using a Dual Polarimetric X-band
Doppler Weather Radar in The Netherlands:
A Case Study

Civil Engineering & Geosciences
Delft University of Technology

Master Thesis

M.H.G. Akerboom

April 1, 2016

Abstract

Hazardous whirlwind and tornado events are uncommon in the Netherlands. Though, the phenomenon is more frequently spotted over the last years, where significant damage is reported. In the United States, literature studies suggest that due to the increase of the Earth's surface temperature tornadoes will become more frequent and intense. This consequence might affect Europe as well. Therefore, a case study is conducted in order to investigate the current technological abilities within the Netherlands in order to protect itself against possible tornado hazards. In this study the development of an EF1 tornado, reaching wind speed between 138-177 km/h, was detected on 03 November 2013 by the high resolution polarimetric X-band radar IDRA. Results have shown that IDRA was able to detect tornado signatures such as hook echo, V-notch and wind shear, 20 minutes prior touchdown. These observations were verified by multiple systems, located near IDRA site, including radar profiles, C-band radars. Moreover, in-situ measurements were available during the evolution of the tornado storm. From this synergy-based analysis, made possible by the Cabauw Experimental Site for Atmospheric Research (CESAR) and the Royal Netherlands Meteorological Institute (KNMI), it was found that their combined efforts can potentially lead to an effective system for early warning detection of tornadoes.

Acknowledgments

This document is the culmination of several months of research work conducted at the Department of Geoscience and Remote Sensing (GRS), in the faculty of Civil Engineering and Geosciences at Delft University of Technology.

I am thankful to the staff of the GRS department, who never hesitated to provide me with insight and resources. Under the guidance of Herman Russchenberg and Ricardo Reinoso-Rondinel, I was given the opportunity to extend my knowledge and to produce this research. I would like to especially thank Herman, who made it possible to combine work from two projects into one thesis. Also I would like to highlight Christine Unal, who was always willing to answer my questions and provide insights and extra data when necessary. Gratitude goes out to Henk Klein Baltink from the KNMI, for providing data which were not available online and who was always extremely obliging during our correspondence.

Lastly, I would like to thank my family, fellow students and friends for their think a long moments, in particular Guy Danon whose everlasting support never faded.

Contents

1	Introduction	1
1.1	Research question	2
1.2	Structure of paper	3
2	Radar applications on weather	4
2.1	S-band, C-band and X-band weather radars	4
2.2	Radar equation	5
2.3	Radar equation for point targets	6
2.4	Radar equation for meteorological applications	7
2.5	Reflectivity factor to rainfall rate	10
2.6	Polarization of weather radars	11
2.6.1	Single polarized Doppler radars	11
2.6.2	Dual polarized Doppler radars	15
3	Tornado development and detection	21
3.1	Tornado development	21
3.2	Tornado detection with use of radars	23
3.2.1	Hook echo	24
3.2.2	V-notch	24
3.2.3	Bounded weak echo region	24
3.2.4	Debris signatures	25
4	Case Study & Data Set	29
4.1	Case date and touch down time verification	29
4.2	Weather predictions and issued warnings	30
4.3	Reported trail of rotating cell and proof and damage by the tornado	31
4.4	Data acquisition & Measurement instruments	35
4.4.1	IDRA, X-band radar	36
4.4.2	TARA, S-band radar	37
4.4.3	Tower in-situ measurements	37
4.4.4	Windprofiler	38
4.4.5	Cloud radar	38
4.4.6	KNMI's C-band radars	39
5	Analysis of high resolution X-band IDRA data	40
5.1	Wind shear signatures verified by spectrum width	40
5.2	V-notch and hook echo	43
5.3	Reconstruction of the touch down time	43
5.4	Specific differential phase	46
6	Case verification with use of additional data sets	47
6.1	KNMI C-band Radar	47
6.2	TARA, S-band radar	49

6.2.1	TARA - zoomed-out storm capture	49
6.2.2	TARA - zoomed-in storm capture	50
6.3	CESAR in-situ tower measurements	52
6.4	35GHz CloudRadar	52
6.5	Wind profiler	53
7	Conclusions	55
8	Discussion & Recommendations	57

List of Figures

1.1	Geographical layout of most damaging tornadoes reported over the years 2008-2015 in the Netherlands	2
2.1	Basic representation of the application of a weather radar	5
2.2	Visualization of a range bin for weather radar applications	8
2.3	Visualisation of a horizontal and dual polarized radar.	11
2.4	Representation of total velocity w.r.t. radial velocity.	14
2.5	Cross sections of falling rain droplets and ice particles	17
3.1	Representation of tornado formation.	22
3.2	A vertical pressure profile of a tornado.	23
3.3	Example of a hook echo	24
3.4	Example of a v-notch signature	25
3.5	Vertical cross section of theoretical Bounded Weak Echo Region (BWER).	25
3.6	Mean Doppler velocity signatures during tornadic activity	26
3.7	Example of debris signatures on a reflectivity and differential reflectivity scan.	26
3.8	Example of tornadic wind shear signatures	27
3.9	Example of tornadic spectrum width signatures.	28
4.1	First twitter message on the tornado at Wijk bij Duurstede, hook echo screenshot by the KNMI	30
4.2	Surface pressure chart of 03-11-2013, issued by KNMI.	31
4.3	Reconstructed path of the rotating cell	32
4.4	Development of the Tornado at Wijk bij Duurstede	33
4.5	Proof of tornado at Wijk bij Duurstede	33
4.6	Damage after the touch down of the tornado.	34
4.7	Schematic drawing of the CESAR site layout	35
4.8	Schematic drawing of IDRA	36
4.9	Schematic drawing of TARA	37
4.10	Aliased and De-aliased TARA velocity images	38
4.11	KNMI C-band radar coverage of the Netherlands.	39
5.1	Partly zoomed PPI of IDRA of radial velocity and spectrum width.	42
5.2	Partly zoomed reflectivity PPI of IDRA.	43
5.3	Full data set of the partly zoomed in radial velocity data.	45
5.4	Partly zoomed PPI of IDRA of specific differential phase and reflectivity.	46
6.1	Composite C-band radar snapshot	48
6.2	De Bilt C-band radar scan at a 0.4° elevation	49
6.3	TARA reflectivity plot of the interval 12:20-13:50 UTC.	50
6.4	TARA plots of reflectivity, Doppler velocity, horizontal wind speed, horizontal wind direction.	51
6.5	Wind speed and direction observed at the CESAR tower.	52
6.6	Measurements of KNMI's 35GHz CloudRadar.	53

List of Tables

1.1 List of most damaging tornadoes over the years 2008-2015 in the Netherlands . . . 2

2.1 Typical weather radar characteristics 5

2.2 Three direct outputs parameters of a conventional Doppler weather radar 12

2.3 Typical Z_{hh} values observed by a horizontal polarized weather radar 12

2.4 Seven direct outputs parameters of a conventional dual polarized Doppler weather radar 16

2.5 Typical Z_{dr} values observed by a dual polarized weather radar (Leon, 2015) . . . 16

2.6 Typical L_{dr} values observed by a dual polarized weather radar (Leon, 2015) . . . 18

2.7 Typical K_{dp} values observed by a dual polarized weather radar 19

3.1 Detectable tornado signatures on weather radars per radar output 23

4.1 Measurement system configuration and technical specifications used on 03-11-2013 35

4.2 Four direct outputs from TARA 37

5.1 Distance traveled and ground speed of the rotating cell based on the movement of IDRA wind shear pixels. 44

Introduction

Tornadoes are a worldwide occurring phenomena and mostly known from their outbreaks in the United States. However, this does not mean that tornadoes are an exclusive phenomena in the United States only. Even though the US reports more than 1000 tornadoes per year, it is interesting to observe that the phenomenon is in the Netherlands with around 10/15 occurrences per annum, a multi annual occurring event as well (KNMI, 2014).

According to a study performed in the United States, tornado development is subject to climate change (Moore & Leduc, 2015). The main driver of this finding is the increase of moist in the atmosphere due to increase of the Earth's surface temperature. That is, due to global warming, more moist is able to reside in the lower troposphere, which could increase the Convective Available Potential Energy (CAPE). CAPE is a measure of the amount of energy available for convection and is directly related to the maximum potential vertical speed within an updraft; thus, higher values indicate greater potential for severe weather.

As found in model projections for North America, a robustly higher CAPE and greater surface moisture are the key factors for an increase in severe convection potential and thus an increase in tornado incidents in the near future. (Diffenbaugh, 2013) (Paquin, 2014)

According to Brooks (2014), the most intense tornadoes increase in frequency over time in the United States, while both tornado density as well as tornado outbreaks intensify consistently as well. This finding should be interpreted as a warning towards Europe, as tornadoes are not considered a severe thread on the continent yet, and therefore no studies are available on the impact of climate change with respect to tornado development.

And even though, damage encountered after a tornado event in The Netherlands is significantly less than in the US, costs can still reach over 1 million Euros (NOS, 2013a), next to the danger it causes for society. A list of the most damaging tornadoes in last 7 years in The Netherlands is presented in table 1.1 accompanied with a geographical representation in figure 1.1. This list is the result of a thorough research conducted online where next to press releases, also confirmations via social media networks were collected.

From table 1.1 and figure 1.1, it can be established that over the past 7 years in the Netherlands 7 hazardous tornadoes were observed. From this time frame, attention is drawn to the last 4 years, thus from 2012 onward. When inspecting the re-occurrence of a reported hazardous tornado event, it can be concluded that every year one case was reported and in 2015 even two.

It can be speculated that this increase in observed hazardous event are subject to climate change.

Table 1.1: List of most damaging tornadoes over the years 2008-2015 in the Netherlands

Date	Location	Reported damage in Euros
August 3rd 2008	Lutjegast Sebaldeburen Doezum	several million
March 1st 2008	Zwolle	Several 100 thousands
June 5th 2012	Montfort	<100.000
November 3rd 2013	Wijk bij Duurstede	Several millions
June 9th 2014	De Moer	<100.000
May 19th 2015	Heusden	Several 100 thousands
August 24th 2015	Wieringerwerf	Several 100 thousands

**Figure 1.1:** Geographical layout of most damaging tornadoes reported over the years 2008-2015 in the Netherlands

However, the upcome of social media networks (think of twitter, facebook and webblogs) are assumed to play a significant role as well in the increase of reported hazardous event, simply because information is easier shared nowadays.

1.1 Research question

It is made clear above, that not much data is available on tornadoes and whirlwinds in general throughout the Netherlands. With the uncertainty of climate change impacts in the future, it is valuable to investigate what the current technological ability is within the Netherlands in order to protect itself against possible tornado hazards. Here it must be made clear that by technological

abilities mainly weather radar applications are meant, as these are the most effective tools for tornado detection. Next to weather radar applications, weather forecast models play a role in the tornado forecasting as well and may be useful for protection to some extent. However, weather forecast models are not the focus of this work.

From historical data it may be stated that tornadoes in the Netherlands are not as violent and strong as they are found in the US (which can also be concluded from the reported damage in table 1.1). The dimensions of these phenomena are smaller too. Where to ground width of a tornado in the US can be of several of hundreds of meters, in the Netherlands no more than several tens of meters in ground width is found. Due to the relatively small dimensions, it is assumed that a high temporal and spatial resolution radar system is necessary in order to observe such an event.

The well maintained high resolution X-band radar IDRA located at the Cabauw Experimental Site for Atmospheric Research (CESAR) observatory in the Netherlands, provides openly available data for research and is operated by Delft University of Technology. CESAR observatory also features many measurement systems for atmospheric applications and is therefore a perfect site to monitor a passing rotating cell which produces tornadoes.

Therefore, a main research question arises:

Can the high resolution X-band radar IDRA detect a typical small scale rotating cell which can produce a tornado?

In order to provide more depth to the the main question the following subquestions are formulated:

- If so, what are the most significant detection signatures found by IDRA?
- If so, what are the signatures observed by additional verifying measurement systems?

1.2 Structure of paper

The report is organized as follows. In chapter 2, a theoretical framework is given where the basic radar principles are explained and attention is paid on how weather radar outputs are obtained and interpreted. In the next chapter the physics behind tornado development are addressed as well as tornadic signatures observed by weather radars. This is followed in chapter 4 by an explanation on the specific case study event and the data sets used for analysis. In chapter 5 results of the high resolution X-band radar are presented which are followed by results of the verifying measurement systems in the next chapter. The conclusion is given in chapter 7 and lastly the discussion and recommendations are presented in chapter 8.

Radar applications on weather

In the 21st century, radars have become a common and indispensable application in every day life. The weather forecast on the 8 o'clock news as well as the 'buienradar app' that everybody directly checks as soon as they see the first rain droplet coming down are all dependent on radars, weather radars in particular. Weather radars are popular due to the fact that they are able to deliver information on precipitation in near-real time. However, weather radars also provide knowledge about storm intensity, type, size, location and direction. With these characteristics, movement and development of significant weather events can be monitored and information can be used.

Weather radar data is mainly used for three applications:

- Short-term and long-term weather forecasts
- Data collection for better numerical weather predictions
- Research and (climate change) monitoring

2.1 S-band, C-band and X-band weather radars

Mainly 3 types of bands are used for radar weather applications: S-band, C-band and X-band. The characteristics of these types can be found in table 2.1.

In weather radar applications, the assumption is made that Rayleigh scattering occurs. This means that the target, in this case the precipitation particle, is small compared to the wavelength. Without going into further detail of this theory it is concluded that short wavelength radars are more effective in detecting small particles such as cloud droplets and drizzle drops, while large wavelength radars are more effective in detecting larger targets.

The target particles absorb part of the energy emitted by the radar when the signal propagates through the atmosphere, while a part is scattered back to the radar. The significant differences in maximum range for the different band types can be explained due to attenuation of the emitted signal mostly by energy absorption of the particles. This is the reason why an X-Band radar (3 cm wavelength) has typically a 6 times smaller range than an S-band radar (10 cm wavelength).

Table 2.1: Typical weather radar characteristics, (Leck, 2009)

Radar band	Wavelength [cm]	Frequency [GHz]	Maximum range [km]
S-Band	10	2.7-2.9	300
C-Band	5	5.25-5.725	200
X-Band	3	9.3-9.5	50

Band selection is mainly a function of the trade offs between range and cost as the magnitude of the wavelength is proportional to its antenna size and therefore installation and maintenance costs. Due to its range characteristics, S-band and C-band radars are mostly used by national meteorological services, installed on multiple strategic locations to provide nationwide coverage. S-band radars are popular in the United States and Russia due to its large range characteristics, while in European countries C-band is most common.

Nowadays, X-band radars for weather applications are becoming more and more popular due to its compactness, easiness of deployment and low cost in comparison with standard S- or C-band weather radars. X-band radars are used for applications such as gap filling in complex terrain, to improve low altitude radar coverage, to conduct research and especially to perform high-resolution precipitation measurement in densely populated areas, in order to improve urban water management and flood prediction. (Unal, 2014) (Fabry, 1994) (Berne, 2004) (Collier, 2009) (Liguori, 2012) (Ochoa-Rodriguez, 2014)

2.2 Radar equation

Radar applications are an active remote sensing technique. This means that first the transmitter sends a signal which is then received, rather than only receiving natural energy that is reflected or emitted from the observed scene. As explained above, the transmitted signal will be partly absorbed and partly scattered back by particles to the antenna. The back scattered signal can then be interpreted for meteorological applications, see figure 2.1.

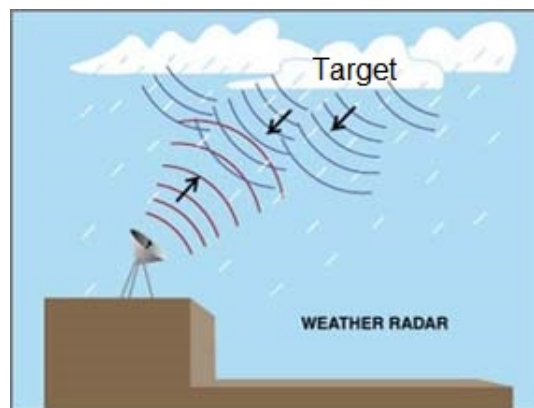


Figure 2.1: Basic representation of the application of a weather radar; pulses are sent out by a transmitter and partly received back. From the received power meteorological interpretations can be constructed.

In order to fully understand how radar output parameters are found, first the radar equation is explained based on (Otto, 2013). Starting with the step by step explanation of obtaining the received power, P_r , scattered back from a point target.

2.3 Radar equation for point targets

The radar equation can be presented as (Probert-Jones, 1962) (Doviak & Zrnica, 2006):

$$P_r = \frac{P_t G_t}{4\pi R_p^2} \frac{\sigma}{4\pi R^2} \frac{G_r \lambda^2}{4\pi} \quad (2.1)$$

This equation can be divided into three parts which will now be explained starting with the most left part of the right hand side of the equation:

$$\frac{P_t G_t}{4\pi R_p^2}$$

The above equation, constructs the so-called power density at the radar target. The transmitted power by the radar, P_t is divided by the surface area of a sphere at first ($4\pi R_p^2$, where R_p is the radius of the sphere at the point target), assuming that the radar transmits its signal in all directions.

Subsequently this value is multiplied with the antenna gain G_t which is taking the antennas efficiency and directivity into account. Thus, describing how much power is actually transmitted in the direction of peak radiation to that of the source. In order to secure a narrow angle and a good resolution of the target, this gain is typically high for weather radar applications.

Now inspecting the middle part of equation 2.1:

$$\frac{\sigma}{4\pi R^2}$$

The just constructed power density which arrives at the target, is multiplied with the monostatic radar cross section (σ). This is the measure of a target's ability to reflect radar signals in the direction of the radar receiver. More elaboration in the radar cross section will be given in section 2.4. Assuming that the target is scattering the signal in all possible directions, this value is then again divided by the equation of the surface area of a sphere.

Lastly the received signal, is depended on characteristic of the receiving antenna; the aperture area of the receiving antenna:

$$\frac{G_r \lambda^2}{4\pi}$$

The aperture area represents how much power is captured from the plane wave and delivered by the antenna. In this formula λ is the emitted wavelength and G_r the gain of the receiver.

Many variables in the radar equation are dependent on a set radar characteristics, which can be combined to one constant, often referred to as the radar constant (C):

$$C = \frac{P_t G_t G_r \lambda^2}{(4\pi)^3} \quad (2.2)$$

2.4 Radar equation for meteorological applications

As mentioned earlier, the previous formulas apply only to a point target. However, in meteorological applications instead of point targets volume targets are used, as clouds consists of many small hydrometeors which are impossible to observe individually.

The term hydrometeor will be extensively used throughout this paper and explicitly means any water or ice particle that has been formed in the atmosphere as a result of condensation or sublimation such as rain droplets, snow or hail.

In order to be able to apply equation 2.1 to a volume, the radar cross section term must be replaced with the sum of all radar cross sections in one volume. This can be done by multiplying the total volume (V) with the sum of the radar cross section per unit volume:

$$\sigma = \sum_{\text{volume}} \sigma_i = V \sum_{\text{unitvolume}} \sigma_i \quad (2.3)$$

For spherical targets, the radar cross section can be divided into 3 region scenarios:

1. Rayleigh region: the target is small compared to the wavelength
2. Resonance or Mie region: the target size has the same order of magnitude with respect to the wavelength
3. Optical region: target is significantly larger than the wavelength

In weather applications the Rayleigh region is used, which means that the Rayleigh scattering approximation of backscattering cross sections for dielectric spheres can be applied (Battan, 1973):

$$\sigma_i = \frac{\pi^6 |K|^2 D_i^6}{\lambda^4} \quad (2.4)$$

Where D is the diameter of the target hydrometeor, λ the radar induced wavelength and $|K|^2$ the dielectric factor depended on the material of the target, in weather applications mainly water.

In mathematical terms the radar cross section is the ratio between the backscattered power divided by the incident power density, thus having m^2 as unit. And in order to obtain a better understanding of this parameter, its dependencies should be stated. The radar cross section is subject to:

- The frequency of the electromagnetic wave
- The geometry/angle of the target
- Electromagnetic properties of target

The volume V in equation 2.3 can be approximated as a cylinder (presented in figure 2.2), where the height is equal one range-bin and θ is the radar beam width.

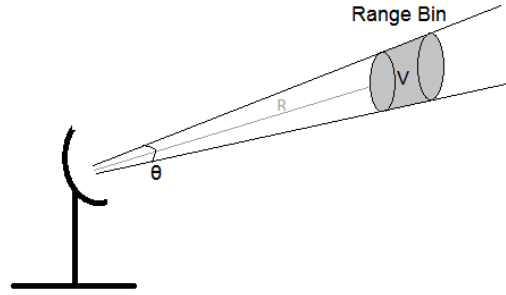


Figure 2.2: Visualization of a range bin for weather radar applications

For frequency modulated continuous wave (FMCW) weather radars, a range bin (Δr) is dependent on the bandwidth of the radar and can be obtained with the following formula, where c is the speed of light and B is the bandwidth:

$$\Delta r = \frac{c}{2B} \quad (2.5)$$

The volume of the cylinder which is equal to the base area (πr^2 , where r is the radius of the base) times its height, one range bin, can therefore be expressed as follows:

$$V = \pi r^2 \frac{c}{2B} \quad (2.6)$$

From this equation the radius of the base r can be rewritten in the distance from the radar to the cylinder R and the antenna beam width:

$$r = (R \tan \frac{\theta}{2}) \quad (2.7)$$

As the antenna beam width in weather applications is fairly small, the tangent function in this equation can be left out as long as the beam width is expressed in radians. After substituting equation 2.7 into equation 2.6, the volume is only expressed in radar specific parameters and the measurement distance:

$$V = \pi R^2 \frac{\theta^2}{4} \frac{c}{2B} \quad (2.8)$$

Before this term is plugged back into the radar equation, it has to be corrected first as the radar signal is not a homogeneous signal and follows a Gaussian distribution. This is done by multiplying equation 2.8 with $\frac{1}{2\ln 2}$ (Probert-Jones, 1962).

Now plugging the obtained volume and radar cross section for meteorological targets back into the radar cross section for a volume (formula 2.3), a new version of the radar equation for a volume target can be set up:

$$P_r = \frac{\pi^3 P_t G_t G_r \sigma^2 c}{1024 \ln 2 B \lambda^2} |K|^2 \sum_{unitvolume} D_i^6 \frac{1}{R^2} \quad (2.9)$$

The radar equation for meteorological volume targets as described above is quite long and when inspecting it closely, features many radar specific values. These values can be separated and expressed in the so-called radar constant term, C :

$$C = \frac{\pi^3 P_t G_t G_r \sigma^2 c}{1024 \ln 2 B \lambda^2} |K|^2 \quad (2.10)$$

This simplifies the radar equation to:

$$P_r = C \sum_{unit\ volume} D_i^6 \frac{1}{R^2} \quad (2.11)$$

Eventually, the main goal of the radar equation is to express the observed precipitation into one single output parameter. In order to achieve this, the parameter called radar reflectivity factor (z) is introduced. This reflectivity factor with unit $\frac{mm^6}{m^3}$ is purely a property of the observed precipitation and described as:

$$z = \sum_{unit\ volume} D_i^6 \quad (2.12)$$

Now by simply substituting the radar reflectivity factor into equation 2.11 and subsequently rearranging it such that the radar constant, the received power and the range to the targeted range bin are a function of this factor, the following formula is found:

$$z = \frac{P_r R^2}{C} \quad (2.13)$$

The just derived radar equation for meteorological volume targets is an approximation, and is therefore based on several assumptions:

- The target hydrometeors are dielectric spheres (e.g. an electrical insulator that can be polarized by an applied electric field)
- All hydrometeors are consisting out of the same material, namely water
- The diameters are small compared to the radar wavelength
- The hydrometeors are distributed homogeneously within a single range-bin
- Multiple scattering among hydrometeors can be neglected
- The main lobe of the radar beam is approximated by a normal distribution

Next to these assumptions, the following restrictions independent of the type of weather radar should be taken into account:

- The radar beam is cone shaped and thus spreads out with distance
- The beam of the radar is straight while the earth has a curvature. The farther away the observations are taken, the higher above the ground they are as well. This mainly is an issue for far range radars, typically C-band and S-band.

Lastly, it should be taken into account that the radar constant in general is always subject to calibration and therefore it is important that the radar is maintained well and checked and calibrated regularly when it is operated.

2.5 Reflectivity factor to rainfall rate

In the previous section the radar equation was manipulated into a suitable equation for weather applications with as a direct output the radar reflectivity factor, z . Reflectivity is a valuable output on its own, but it can also be converted into rainfall rate R , which has as unit [mm/hr]. Rainfall rate is a function of raindrop-size distribution $N(D)$ within a unit volume. This raindrop-size distribution is assumed to have an exponential relationship with reflectivity z and is expressed in equation 2.14 (Battan,1973).

$$z = \sum_{unit\ volume} D_i^6 \equiv \int_0^{\infty} D^6 N(D) dD \quad (2.14)$$

Subsequently, the quantity called liquid water content (LWC) per bin volume can be formulated:

$$LWC = \frac{\pi}{6} \int_D D^3 N(D) dD \quad (2.15)$$

Where the raindrop size distribution can be approximated with many relations, for example:

$$N(D) = N_0 e^{-\Lambda D} \quad (2.16)$$

In equation 2.16, N_0 is the raindrop concentration in $m^{-3}mm^{-1}$ and Λ is the slope parameter of the raindrop-size distribution/raindrop diameter curve in mm^{-1} .

When simply multiplying the liquid water content per bin volume with the terminal fall velocity, the rain rate in mm/hr can be found. From obtained experimental data a relationship between the LWC times terminal fall velocity, thus the rain rate and the reflectivity is constructed. This power-law relationship is founded by Marshall and Palmer and can be found in equation 2.17 (Marshall, 1948).

$$z = aR^b \quad (2.17)$$

Often as a first approximation $a=200$ and $b = 1.6$ is used, though an extensive range of relations of this kind do exist and are subject to precipitation type and intensity. (Uijlenhoet, 2001)

2.6 Polarization of weather radars

The just explained radar equation, is focused on the most elementary and basic output: the equivalent reflectivity factor Z or sometimes known as Z_{hh} . However, the reflectivity factor is not the only output of a weather radar as dependent on the type of radar, different outputs are available. At the moment there are mainly two types of weather radars in use by meteorological institutes and research centers:

- Single polarized Doppler radars
- Dual polarized Doppler radars

The difference between these two type of radars is fairly simple. A single polarized Doppler radar, also known as a conventional Doppler radar transmits and receives exclusively horizontal pulses, providing one dimensional information about the target. A dual polarized Doppler radar is able to transmits pulses at horizontal and vertical polarization and receives back in an horizontally and a vertically polarized channel. A visualization of both single and dual polarized radar application are presented in figure 2.3. Both applications and its radar outputs are discussed in the following sections.

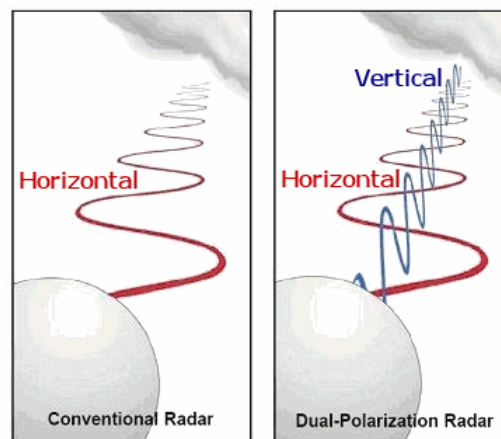


Figure 2.3: Visualization of conventional (horizontal polarized) radar application with respect to a Dual Polarization (vertical and horizontal polarized) radar. Source: roc.noaa.gov

Radar outputs of horizontal scanning radars are generally displayed on a plan position indicator (PPI). A PPI is a polar coordinate display of the area surrounding the radar platform, where the radar is located in the origin of the display.

2.6.1 Single polarized Doppler radars

A single polarized Doppler weather radar uses next to the conventional power of signal send/return measurements, frequency shifts as information. The Doppler effect induced in the backscattered signal can be used to produce velocity data about meteorological scatterers within a range bin. Also with use of the frequency of the returned signal a measure of velocity dispersion per range bin can be provided.

A single polarized Doppler radar has 3 direct outputs which are listed in table 2.2 and will be elaborated on directly after in the same sequence as they are presented in the table.

Table 2.2: Three direct outputs parameters of a conventional Doppler weather radar

Output parameter	Description	Unit
Z_{hh}	Co-polarized equivalent reflectivity factor at horizontal polarization	dBZ
V_{hh}	Mean Doppler radial velocity	m/s
W_{hh}	Doppler spectrum width	m/s

2.6.1.1 Horizontal Reflectivity

Horizontal reflectivity, Z or Z_{hh} is the most basic and easy interpretable radar output. It is generally the first output meteorologists turn to when inspecting data from a radar scan. Reflectivity is obtained by transmitting a horizontal polarized wave (Z_{hh}) and which is also received back in the horizontal plane (Z_{hh}).

The radar reflectivity factor z , which is found in section 2.4, equation 2.13, can vary significantly over a large range, and is therefore expressed on a logarithmic scale with unit dBZ:

$$Z = 10 \log_{10} \left(\frac{z}{1 \text{mm}^6/\text{m}^3} \right) \tag{2.18}$$

Reflectivity values typically range between 0 and 65 dBZ. Negative values are classified as non-meteorological scatterers or (ground) clutter. Low reflectivity can be interpreted as light rain and as the reflectivity increases the precipitation intensity does so too. High reflectivities mainly mean heavy precipitation, falling melting ice particles or hail, that with their wet outer surface look like very large raindrops. (Uijlenhoet, 2001)

Typical reflectivity values are listed in table 2.3.

Table 2.3: Typical Z_{hh} values observed by a horizontal polarized weather radar

Weather type	Typical reflectivity [dBZ]
Mist/clouds	<15
Light rain	15 - 25
Moderate rain	25 - 35
Showers	35 - 45
Heavy precipitation	45 - 55
Thunderstorms	>55
Hail - size increasing with reflectivity	55- 65

2.6.1.2 Mean radial Doppler velocity

The mean radial Doppler velocity enables meteorologists to monitor movements of particle within precipitation clouds. This can be done by determining the frequency shift through measurements of the phases change that occurs in waves during a series of pulses. A frequency shift can be observed in a wave when targets have a positive or negative motion in the line of sight of the radar beam. For the explanation of the this parameter, lecture slides by Leon (2015) are used.

In order to obtain the radial velocity from the frequency shift, first the relationship between the initial transmitted phase Φ_0 and the return phase Φ_D has to established:

$$\Phi_D = \Phi_0 + \frac{4\pi r}{\lambda} \tag{2.19}$$

Where the term $\frac{4\pi r}{\lambda}$ represents the total distance traveled ($2r$) in wavelengths (divided by λ) and in radials (time 2π).

The difference of the phase over time is then:

$$\frac{d\Phi_D}{dt} = \frac{4\pi}{\lambda} \frac{dr}{dt} \quad (2.20)$$

The Doppler frequency shift has the following relation with the Doppler phase shift of the signal:

$$\Delta f = \frac{1}{2\pi} \frac{d\Phi_D}{dt} \quad (2.21)$$

And therefore:

$$2\pi\Delta f = \frac{4\pi}{\lambda} \frac{dr}{dt} \quad (2.22)$$

Which results in:

$$\Delta f = \frac{2v}{\lambda} \quad (2.23)$$

This equation can be rewritten in order to directly find the radial velocity from the measured frequency shift:

$$v_r = \frac{\Delta f \lambda}{2} \quad (2.24)$$

As every particle in the volume bin has its own velocity vector, the backscattering signal is a combination of all these velocities. The main contributor to Doppler velocity is horizontal wind (as the frequency shift is mainly induced by radial velocity, e.g. movements from and towards the radar) and its variations. Next to wind, the radial velocity is also dependent on other conditions such as antenna motion, changes in vibrations and- or orientations of hydrometeors, turbulence, wind shear and differences in fall speed. (Doviak & Zrnice, 2006)

It must be taken into account that mean radial Doppler velocity is not the same as the total velocity of the hydrometeors. The radial velocity is only sensitive to particle movement in the direction of the radar beam. This means that only the vector component away or towards the radar beam of the total velocity of the hydrometeors is registered. The radar makes a 360 degree turn during its scan, which means that all possible velocity directions are captured such that from inspecting the complete radar PPI, the general wind direction can be determined.

The mean Doppler velocity is also a function of elevation angle of the radar scan. Hydrometeors follow their own velocity pattern and when the radar angle is set at an certain elevation, an offset in measurements might be introduced. See figure 2.4 for an example of such a case, here the particle velocity is assumed to be in the same direction of the radar beam's line of sight. This

will only give significant differences in velocities when the scan elevation is high, in case of low scan elevation angles no correction with respect to beam elevation angles has to be made.

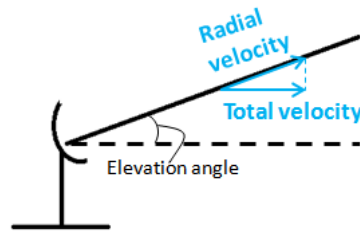


Figure 2.4: Representation of total velocity assumed to be in the direction of the line of sight of the radar, with respect to the radial velocity measured by the radar. Note that with high scan elevations, corrections has to be implemented to correct for the elevation angle.

The radial Doppler velocity is bounded to a maximum measurable velocity called the Nyquist velocity. When true velocities are larger or smaller (as Doppler velocity has an equal positive and negative spectrum range), values will be aliased back into the unambiguous range.

Aliased data basically means that the real wind velocity is higher than the maximum velocity that can be measured by the system, also known as Nyquist velocity. In the case that a higher velocity than the Nyquist velocity is present, the velocity wraps around the other end of the measurement palette, registering an abrupt drop in the measurement. For example, if the Nyquist velocity is 100 km/h and the particles are moving with 110 km/h towards the radar, its recorded velocity is then registered to be -90 km/h away from the radar.

As two measurements per wavelength are needed to determine a frequency, therefore the phase change between the pulses must be less than half the wavelength. So ultimately, the pulse repetition frequency (PRF) of a radar determines the maximum speed that can be detected without confusion.

The Nyquist velocity is per radar unique and can be calculated by the following formula (see Battan (1973) for the derivation of the equation):

$$V_{max} = \frac{PRF\lambda}{4} \quad (2.25)$$

As the inverse of the pulse repetition frequency is equal to the sweep time (T_s), the Nyquist velocity can also be expressed in an alternative form:

$$V_{max} = \frac{\lambda}{4T_s} \quad (2.26)$$

Aliased data can be corrected for by multiply it by minus twice the Nyquist velocity:

$$V_{corr} = V_{wrapped} \cdot -2V_{Nyquist}^{max} \quad (2.27)$$

2.6.1.3 Spectrum width

Within one radar sample volume, millions of raindrops are present and all having their own velocity vector. This variability in movement in the flow per range bin is expressed in a parameter called spectrum width. Spectrum width is a function of wind shear, turbulence, antenna motion and range of terminal fall speeds of scatterers and of course the quality of velocity samples play a role as well.

A Doppler spectrum is defined as power weighted velocity distribution within the radar resolution volume. A Gaussian-shaped Doppler spectrum (Doviak & Zrnic, 2006) is typically assumed for weather signals and can be fully characterized by its three spectral moments of signal power, mean velocity, and spectrum width. The spectrum width can be found by computing the variance of the Doppler power spectrum.

Large spectrum width values indicate the presence of strong turbulence and/or large wind shear. When the air conditions are very homogeneous or in other words, when stable wind from one direction or still air is present the spectrum width is expected to be small.

It is a less popular parameter than reflectivity and Doppler velocity due to the difficulty in relating standard deviations to meteorologically significant phenomena. Also the fact that values are easily corrupted (e.g., by overlaid echoes), and thus spectrum widths are less reliable and more risky to use (Fang, 2004).

2.6.2 Dual polarized Doppler radars

For conventional radars, spherical hydrometeors are assumed as the radar beam is single polarized. However, in reality this is not the case since hydrometeors vary in appearance significantly. The difference in geometry of hydrometeors is one of the main motivations for the usage of a dual-polarized Doppler radar. A dual-polarized radar, with its two channel antenna is able to transmit and receive both horizontal and vertical components and is therefore able to obtain more information about the targets.

This means that in addition to horizontal reflectivity, Doppler velocity and spectrum width 3 direct extra outputs are available from a dual polarized radar, the linear depolarization ratio, differential reflectivity and differential phase and one indirect one which can be obtained by processing the differential phase: the specific differential phase. All 7 radar outputs can be found in table 2.4 which will be addressed at the end of this section in the same order as presented. In order to provide some feeling for numbers, typical values for polarimetric radar outputs are provided. These typical values hold for S-band radars, when working with radars that operate at a different wavelength, these values may vary slightly. The already discussed parameters reflectivity, mean radial Doppler velocity and spectrum width will not be addressed again as the theory and technique are the same for dual polarized radars.

First, in order to completely understand the concept of dual polarization on weather application, a short elaboration is given on hydrometeor appearances and its application on dual polarized weather radars.

2.6.2.1 Hydrometers observed by dual polarized radars

Indicates above, raindrops in reality are not necessarily spherical. They generally have an oblate shape, where the oblateness increase with raindrop size. Ice particles vary in geometry too, such as plates or columns, while hailstones appear more spherical and irregular shaped.

Table 2.4: Seven direct outputs parameters of a conventional dual polarized Doppler weather radar

Output	Description	Unit
Z_{hh}	Co-polarized equivalent reflectivity factor at horizontal polarization	dBZ
W_{hh}	Spectrum width	m/s
V_{hh}	Mean radial Doppler velocity for transmitted horizontal polarization	m/s
L_{dr}	Linear depolarization ratio	dB
Z_{dr}	Differential reflectivity	dB
Φ_{dp}	Differential phase	deg
K_{dp}	Specific differential phase	deg/km

Representation of rain drops, ice particles and hail shapes can be found in figure 2.5. (Beard & Chuang, 1987)

Since a falling raindrop has an effective larger horizontal cross section with respect to the vertical, the travel time for the horizontal wave to pass through a raindrop is longer than for the vertical wave sent out by the dual polarized radar. This means that a difference in the backscattered signal with respect to horizontal and vertical waves can be observed, which is the mean theory behind the polarized output parameters. With this application the difference in geometry and size can be determined. Thus providing additional information, which enables meteorologists to make a distinction between rain, snow, hail and non-weather items and also between the intensity of the precipitation. The three different direct output parameters in addition to one indirect output parameter from dual-polarized weather radars will now be discussed.

2.6.2.2 Differential Reflectivity

Differential reflectivity Z_{dr} is represented by the subtraction of the horizontal submitted and received component (Z_{hh}) by the vertical submitted and received component (Z_{vv}):

$$Z_{dr} = 10\log_{10}(z_{hh}) - 10\log_{10}(z_{vv}) = Z_{hh} - Z_{vv} \quad (2.28)$$

This parameter is sensitive to differences in horizontal and vertical geometry of hydrometeors and has values typically ranging between -2 and 6 with decibel as unit. High reflectivities represent a large difference between the horizontal and vertical cross section of hydrometeors and therefore very likely represent large raindrops thus heavy precipitation, while low reflectivities are associated with small rain drops or drizzle. As hail is mostly rather spherical, its corresponding Z_{dr} value is expected to be near or around zero dB, while ice crystal depending on their orientation range through the entire spectrum. Typical differential reflectivity values presented in table 2.5.

Table 2.5: Typical Z_{dr} values observed by a dual polarized weather radar (Leon, 2015)

Weather type	Typical differential reflectivity [dB]
Rain with increasing drop size	0 - 6
Hail/graupel with increasing wetness	-1.5 - 2
Snow, wet to dry	-0.5 - 2
Ice crystals, aggregates	-1.5 - 0.5
Ice crystals, vertically to horizontally oriented	0.5 - 5

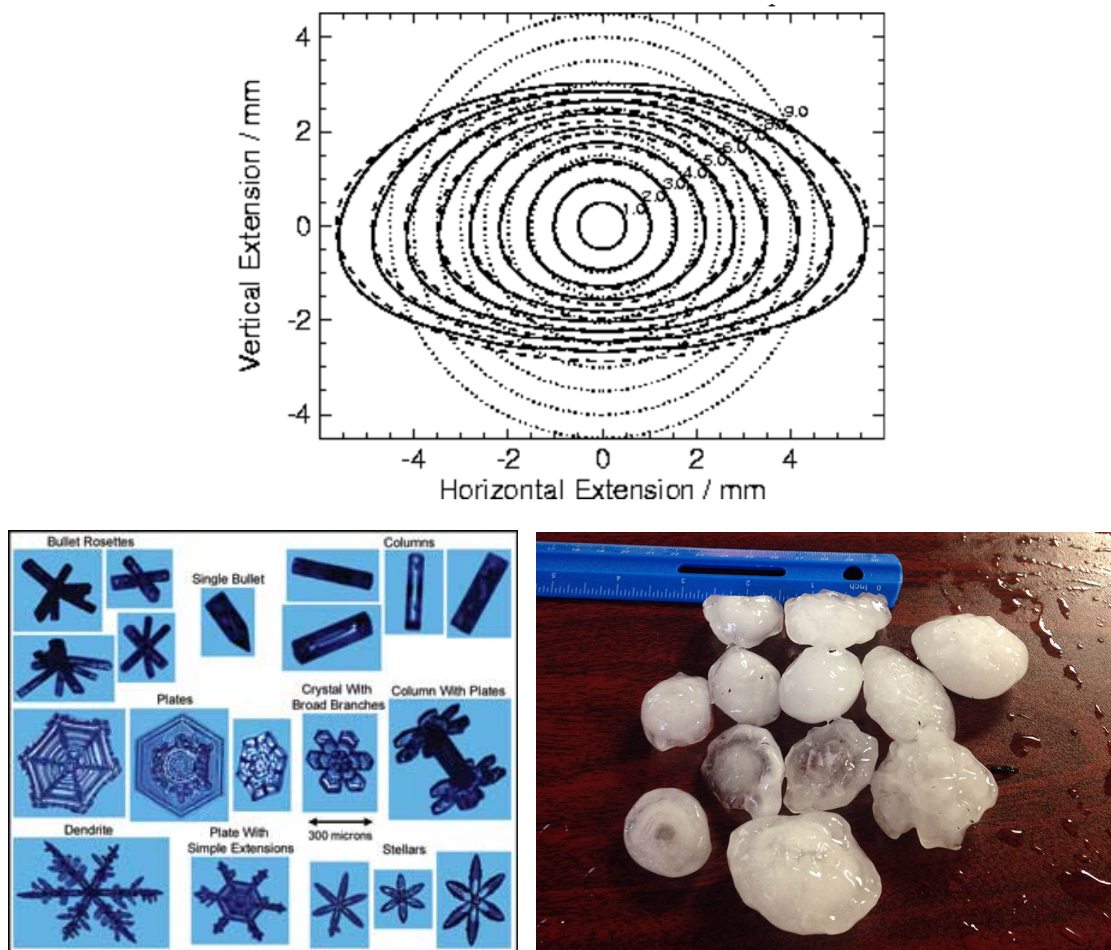


Figure 2.5: Top: Cross sections of falling rain droplets, equivalent volume spheres (dashed line) and spheroids (dotted line) are given for reasons of comparison, (Chuang, 1990). Bottom: Different shapes and sizes of ice particles (left) and the more spherical representation of hail (right)

Applications of differential reflectivity are used to identify areas of increasing median rain drop sizes, areas of aggregation of dry snow and updraft detection when applying a vertical scan. Also it is a valuable parameter when combining analysis with reflectivity observations. For instance rain media can be easily detected when $Z_{dr} \geq 0.5$ dB and the $Z_{hh} \leq 60$ dBZ criteria is met and hail is detected while $Z_{dr} \approx 0$ dB or marginally negative and $Z_{hh} \leq 45$ dBZ (Aydin & Balaji, 1986), (Doviak & Zrnica, 2006), (Lopez & Aubagnac, 1997) and (Straka & Zrnica, 1993).

Next to this, Z_{dr} is used in tornado observation studies as debris tracking mechanism, for debris mostly have very irregular shapes (Ryzhkov, 2005) and (Tanamachi & Hardwick, 2012)

2.6.2.3 Linear depolarization ratio

Linear depolarization ratio (L_{dr}) is the ratio between the cross polarization reflectivity Z_{hv} (vertical polarized backscattered power measured from a horizontal polarized induced wave) and of the vertical co-polarized reflectivity Z_{vv} .

$$L_{dr} = 10 \log_{10}(z_{vh}) - 10 \log_{10}(z_{hh}) = Z_{vh} - Z_{hh} \quad (2.29)$$

The linear depolarization ratio ranges between -35 to -10 dB and is particularly sensitive to frozen hydrometeors, especially with high bulk density and water coatings.

Low L_{dr} values are identified as light rain, cloud droplets and dry ice particles while large values are related to tumbling, wet and non-spherical particles: wet graupel, melting aggregates, hail. In table 2.6, typical L_{dr} values are presented.

Table 2.6: Typical L_{dr} values observed by a dual polarized weather radar (Leon, 2015)

Weather type	Typical linear depolarization ratio [dB]
Heavy rain	>-25
Hail and rain mixtures	-20 - (-10)
Wet snow	-13 - (-18)

As L_{dr} is particularly effective to detect frozen hydrometeors, it is often used to determine characteristics of the bright band within a cloud (the layer in a cloud where frozen hydrometeors reach a melting point), (Zrníc & Matejka, 1993) and (Vivekanandan & Raghavan, 1990) and used as cut-off parameter to ensure good data quality for specific differential phase processing, (Otto, 2011).

2.6.2.4 Differential phase

Induced by the radar, horizontal and vertical pulses are sent through a medium. Subsequently, these pulses are slowed down due to interaction with this medium. This change in phase with respect to the horizontal and vertical polarized component is described with the parameter called differential phase. The differential phase is simply a subtracting of the vertical phase shift from the horizontal phase shift:

$$\Phi_{dp} = \Phi_{hh} - \Phi_{vv} \quad (2.30)$$

Φ_{dp} is then the cumulative differential phase shift for the total round trip between the radar and the resolution volume.

The differential phase shift is a cumulative parameter, this means that per radial a continuous line is produced. The larger the horizontal phase with respect to the vertical phase in a range bin, the faster the phase shift increases. This works in the same way around for a declining phase shift; the vertical phase per range bin is larger than the horizontal phase. In the presence of spherical particles or voids the phase shift remains constant over its range, thus a flat curve can be observed.

Differential phase shift has almost the same characteristics as the differential reflectivity except that it is dependent on particle concentration. The parameter can be deceiving, as it is dependent on both particle concentration and drop size. Meaning that in the case of large drops but low concentration of droplets, the value can also be interpreted as small drops with a high concentration of droplet. This is why differential phase shift results should always be verified with other radar outputs such as reflectivity.

2.6.2.5 Specific differential phase

The specific differential phase, K_{dp} is an indirect output of a dual polarized weather radar as it cannot directly be generated from its direct observations. K_{dp} is basically the range derivative of the differential phase shift along a radial and therefore provides more directly interpretable information. Generally the same theory of the differential phase applies to the specific differential phase concerning data interpretation, when keeping the differential factor in mind. Several methods are available in order to construct the specific differential phase parameter (Sachidananda, 1986), (Gorgucci, 1999), (Wang, 2009) and (Otto, 2011). In this report the method and algorithms by (Otto, 2011) are used.

K_{dp} values typically range between -2 to 7 degrees per kilometer. The same principle to interpret the data is handled as with the differential phase only now in derivative form. Positive K_{dp} values mean that the horizontal polarized pulse is slowed down more than the vertical one. Zero K_{dp} means either no precipitation or spherical particles and negative values means a majority of vertically oriented hydrometeors which are mainly hail, graupel or ice crystals. Typical values for specific differential phase are presented in table 2.7.

Table 2.7: Typical K_{dp} values observed by a dual polarized weather radar

Weather type	Typical specific differential phase [deg/km]
Rain with increasing intensity	0 - 7
Hail/graupel with increasing wetness	-0.5 - 1
Snow, dry to wet	0 - 0.5
Ice crystals from vertically to horizontally oriented	-1 - 0.75

K_{dp} is best used to detect areas of heavy rain and heavy rain mixed with hail. Areas of heavy rain will typically have high K_{dp} due to the large size and concentration of the drops. Warm and cold rain processes is also specifically mentioned as in some cases at areas where high reflectivity values are found, there might be different (unexpected) K_{dp} values present, as a warm rain process produces for instance smaller drops but higher concentrations.

The specific differential phase has some significant advantages compared to for instance the differential reflectivity as K_{dp} :

- Independent of receiver/transmitter calibration
- Independent of attenuation
- Less sensitive to variations of size distributions (compared to reflectivity)
- Immune to partial beam blocking

It can be concluded that the implementation of specific differential phase on storm data, analysis can significantly improve precipitation estimates and hydrometeor identification (Sachidananda & Zrnic, 1986). Next to the just mentioned characteristics, K_{dp} is also a valued parameter due to its ability to successfully reconstruct reflectivity signals after beam blockage (Giangrande & Ryzhkov, 2005).

It must be noted that for the construction of K_{dp} good data quality is required and thus not all data measured by the radar can be used for processing.

The first limitation is that the specific differential phase will become noisy in areas of low signal-to-noise ratios e.g. values lower than 25 dBZ. Thus, K_{dp} is mainly reliable around the core of storm where high reflectivities are found. Subsequently, K_{dp} can only be calculated for range

bins where reflectivity values are larger than 0 dBZ and where the linear depolarization ratio is lower than -15 dB, in order to ensure presence of meteorological scatterers. This means that some data must be discarded from the set before processing. Lastly, total extinction is checked by inspecting the continuity of the differential phase shift. Whenever the signal to noise ratio is too low the data will not be taken into account for further processing.

In case of presence of large Z_{dr} drops along the radial of the data, these parts will not be taken into account for further processing.

Tornado development and detection

The word 'tornado' is originated from the latin word 'tornare' which means turn. This is exactly what a tornado is; a powerful rotating mixture of wind and thunderstorm clouds extending in a funnel shape.

In order to understand how such a funnel shape and thus a tornado can develop, a detailed theory of the physics behind tornado development is first given in this chapter. This is followed by an overview of tornado signature detection with use of weather radars.

3.1 Tornado development

Tornadoes can only develop under specific atmospheric circumstances. To start, the vertical temperature profile of the environment must feature large instabilities. This means that at some points the air at ground level is heated and remains warmer than its surrounding air such that the air experiences convection. This process can be enforced when the air at the ground possesses a high concentration of water vapor, such that the raising parcel will cool even less fast while rising than its surrounding dry air.

Next to this, in order to have a situation with the largest possible temperature difference between this just mentioned parcels and its surroundings, the atmospheric lapse rate of the surrounding air should be high. Such that a strong negative temperature gradient is present (fast temperature decrease with increasing altitude), in order to enable the warm parcels to rise faster. The presence of (very) dry conditions in the upper air layers supports this negative temperature gradient, as during a storm development, upper air is being lift and will cool down following a dry-adiabatic lapse rate (typically 9.8°C per kilometer, which is in theory the most negative temperature gradient), resulting in an even colder higher upper layer.

Subsequently, in this area of large instabilities, a meso-cell will have to present. A meso-cell is a large rain bearing (thunder) storm that advances in cold fronts and due to instable air layers causes a plateau-like low pressure area as the air is pushed away from the cloud top while rising. Due to its substantial size and significant time of existence, a cyclonic rotation within the meso-cell may develop introduced by the Coriolis force (the force introduced by the Earth's rotation).

The final requirement is the presence of strong jet streams within the meso-cell. Jet streams are relatively narrow bands of strong wind in the upper levels of the atmosphere and follow the boundaries between hot and cold air.

Now that the atmospheric requirements for tornado development are laid out and assuming they are present, the formation of a tornado itself can be explained.

As just established, warm parcels with a high concentration of water vapor may locally rise with high velocities within the meso-cell. Due to this rise, a warm air column which can be compared to a chimney with a large pull is developed. As a result from the rotating depression supported by the jet stream, the air which is sucked into this column features a weak torsion.

The law of conservation of angular momentum states that the radius of a rotating column decreases while the speed increases. Meaning that the beginning of the funnel which is induced by the rotating meso-cell is increasing in speed while becoming smaller in diameter.

As the pressure right underneath the developing funnel drops due to the suction, higher concentrations of water vapor will be drawn to these low pressure locations, resulting in a altitude drop of the cloud deck of the preliminary funnel which also again supports updraft of warm air. This process repeats itself as a small part of the cloud base slowly grows into a tornado until it hits the ground. An explanatory picture, of tornado formation is presented in figure 3.1.

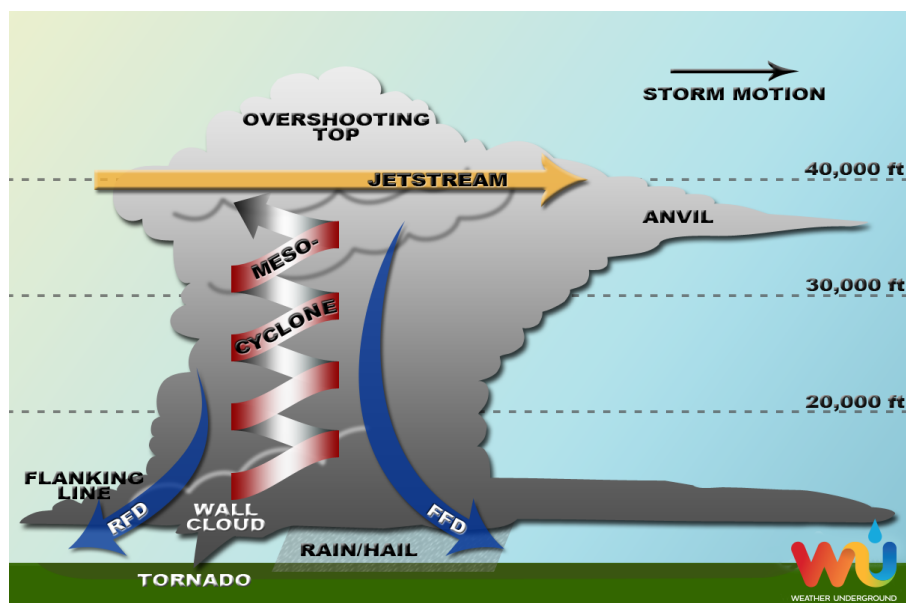


Figure 3.1: Representation of tornado formation. Air is sucked in at the bottom of the funnel and transported upwards creating a strong pressure gradient with its surroundings. The RFD stands for rear flank downdraft and the FFD stands for forward flank downdraft, which are the downdrafts surrounding the updraft. Source: wunderground.com

The isobars of the area where the funnel develops, which under normal circumstances have a wavy horizontal course, are in the case of a tornado touch down following a funnel pattern, expanding underneath the cloud layer. When touch down is reached a very large difference in pressure gradient is evolved; as is presented in figure 3.2, the isobars are very close to each other and the difference in air pressure in the center of the gust with its direct environment can be over 100hPa. This large pressure difference in combination with the high wind speed are the most important factors that determine the strength, lifetime and potential damage incurred by the tornado.

As significant difference between a tornado and whirlwinds exist. A tornado is a violently rotation column of air that is in contact with both the surface of the Earth and a cumulonimbus cloud, or in rare cases, the base of a cumulus cloud. Tornado wind speeds vary from 18 m/s for the weakest up to 135 m/s or greater for the most violent. The key difference between a tornado and a whirlwind is that tornadoes form in a cumulus cloud and descend to the surface of the

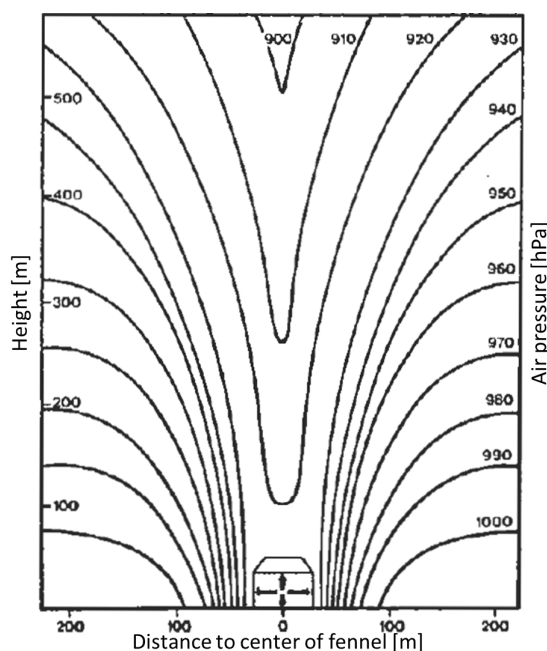


Figure 3.2: A vertical profile of a tornado, showing its isobars. The air pressure gradient is largest just outside the center of the fennel. (Zwart, 1994)

Earth, whereas whirlwinds form at the surface of the Earth and ascend to a cumulus cloud if present. (NOAA, 2014)

3.2 Tornado detection with use of radars

Detection of tornado signatures is a widely studied topic in the research field and Doppler weather radar has proven to be an effective tool (Zrnice & Burgess, 1977), (Zrnice & Istok, 1980) (Bluestein & Unruh, 1989), (Bluestein & Spehger, 1993), (Wurman, 2000), (Tanamachi, 2012). Specific signatures can be found on radar images when an event of this sort is passing by.

Based on the literature above, an overview is presented on what typically can be found when analyzing tornado events with a weather radar.

As explained in the previous section, a tornado consists of a fast rotating fennel accompanied by large cloud deck. When inspecting a radar PPI of outputs during a passing tornado, multiple signatures can be recognized, (Ryzhkov, 2005). The signatures are listed in the table directly below and described in the following sections according to the order of appearance.

Table 3.1: Detectable tornado signatures on weather radars per radar output

Signature	Radar output
Hook echo	Reflectivity
V-notch	Reflectivity
Bounded weak echo region	Reflectivity/Doppler Velocity
Debris at tornado location	Reflectivity/Differential Reflectivity
High wind shear at tornado location	Doppler Velocity
Large turbulence and distribution velocity	Spectrum Width

3.2.1 Hook echo

The most known and famous tornado signature is the hook echo, see figure 3.3. This hook-like feature occurs when winds circling the meso-cell are strong enough to wrap precipitation around the rain-free updraft area of the storm and thus basically leave a visible trail behind the tornado. This signature can directly be detected on a reflectivity scan of a radar and describes a pattern that looks like a hook where its name adapted from.

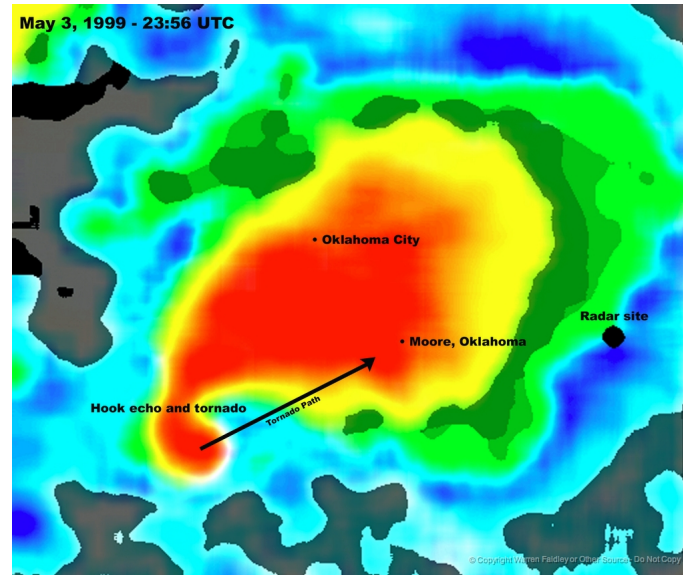


Figure 3.3: Hook echo of a strong tornado passing by the state Oklahoma in the United States on the 3rd of May, 1999. The high reflectivities are associated by red and declining via yellow, green to the lowest values in blue.

3.2.2 V-notch

The V-notch or 'Flying Eagle', is a v-shaped pattern that can be found in the upper part of the precipitation shield, which is in most cases North-East of the hook echo. This phenomenon only occurs when the cloud is that tall that the upper levels of the wind are forced to deflect around the core of the storm and thus spreading the precipitation outward. This pattern is not necessary always present during a tornado case as it only develops in the case of strong and tall super cells. A V-notch can be detected in a radar reflectivity scan where an example is given on in figure 3.4.

3.2.3 Bounded weak echo region

A bounded weak echo region (BWER) can be best observed when inspecting a vertical radar cross section of the tornado storm. It signifies a vertical channel of a weak radar echo region, surrounded by significant stronger echoes. It occurs when precipitation wraps around the warm, moist updraft; due to the strong rotation of the updraft, precipitation cannot fall through it, causing a region of low reflectivity within the fennel, surrounded by high reflectivities. See figure 3.5 for an example of a vertical radar cross section which features a schematic drawing of a BWER.

The bounded weak echo feature is accompanied by specific signatures in the vertical velocity field. Within the bounded weak echo region, large vertical wind shear is present, namely the

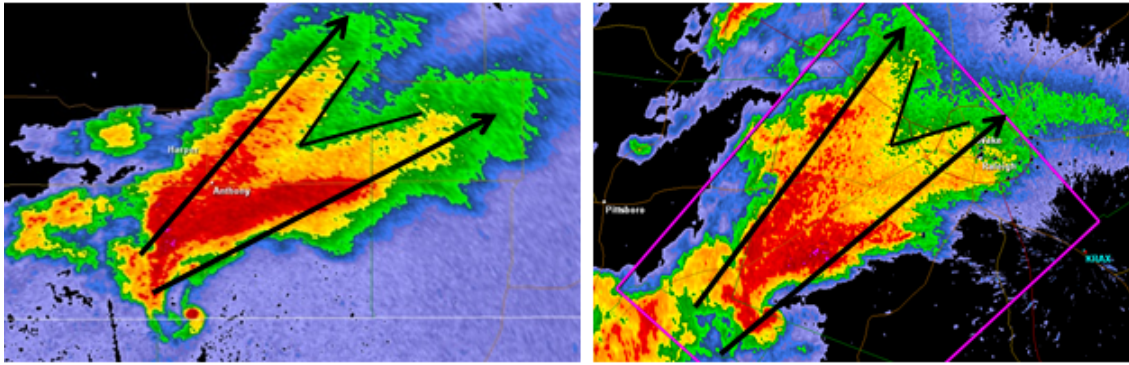


Figure 3.4: A v-notch signature, indicated by the black arrows. The left tornado signature was recorded at the state of Oklahoma in the United States on the 14th of April, 2012, while the right is from state the of North Carolina, on April 16th, 2011.

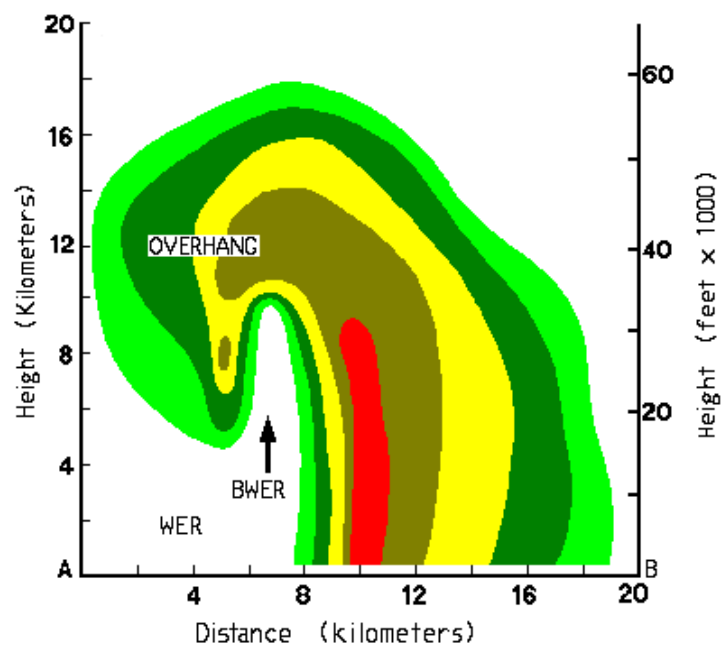


Figure 3.5: Vertical cross section of theoretical echo overhang above the weak echo region (WER), the bounded weak echo region is capsuled by regions of high reflectivity.

tornado fennel with its 'chimney pull effect' which is typically surrounded by two downdraft regions. An example of this vertical wind shear can be seen in figure 3.6.

3.2.4 Debris signatures

Tornadic debris are composed of random oriented particles with irregular shapes. The refractive index of these particles are very different from that of hydrometeors. These differences thereby produce distinctive signatures within radar scans than hydrometeors.

Due to the heavy winds, non-meteorological scatterers such as natural ground covers (trees, grass, etc.), biological scatterers (insects, birds, etc) and man made objects are lifted and spinned randomly oriented through the hydrometeors. A typical debris ball is shown on the radar as an area of high reflectivity on the end of the hook echo, due to the random orientation of the debris

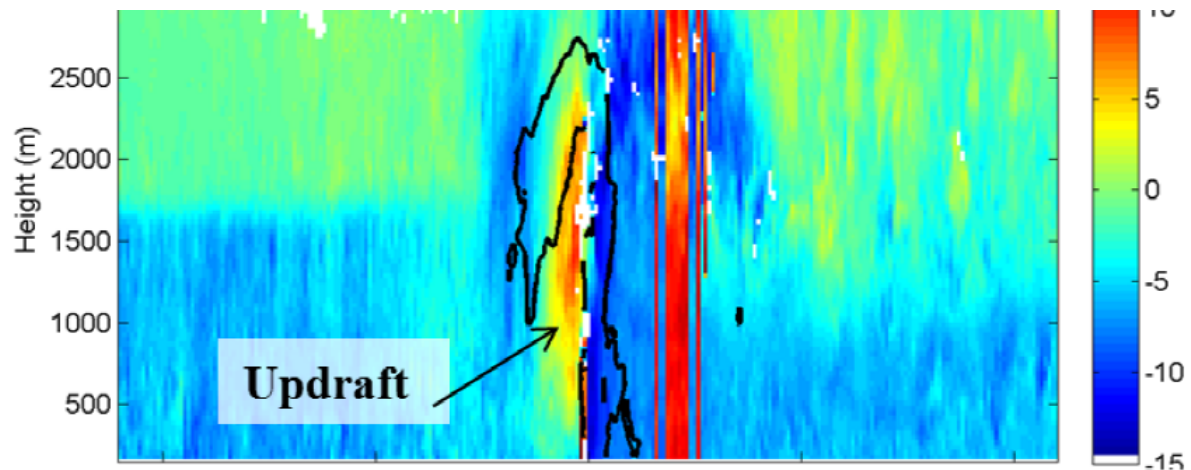


Figure 3.6: Mean Doppler velocity exhibiting an updraft surrounded by two downdraft regions, the black contour lines indicate a 35 dBZ reflectivity boundary, which illustrates the overhang very well. The signature was recorded on 3 January, 2012 in The Netherlands at Cabauw. The case was a convective squall line showing similar signatures to those of tornadic super cells. Figure adapted from (Reinoso-Rondinel, 2014).

particles the differential reflectivity is observed to range around zero, see figure 3.7

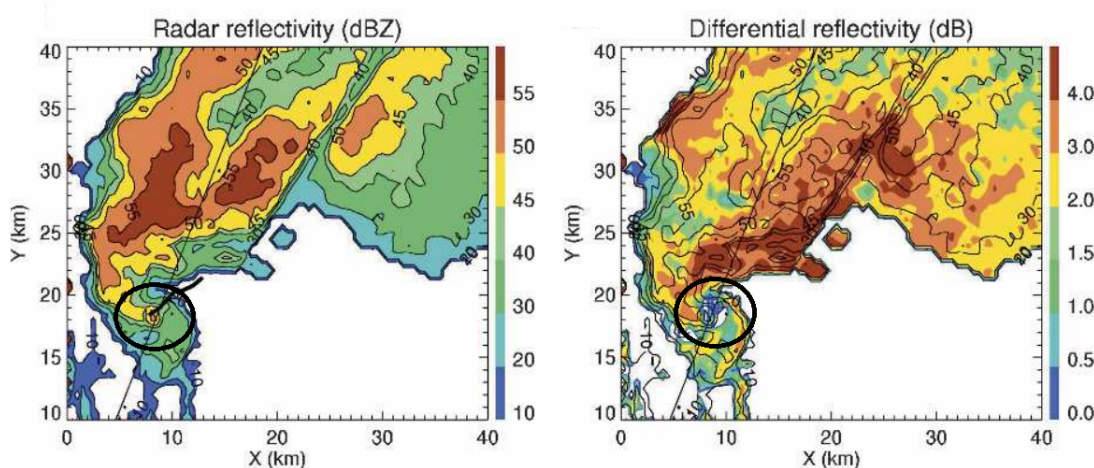


Figure 3.7: Reflectivity and differential reflectivity screen shot of the destructive F4 tornado which hit Moore, Oklahoma in the United states on 8 May, 2003. The debris ball lays within the black circle where on the reflectivity scan, high reflectivities are present, while on the differential reflectivity scan an area of around zero decibel can be observed. Figure adapted from (Ryzhkov, 2005)

Subsequently, the linear depolarization ratio is expected to be significantly higher than typical hydrometeors would produce due to the very large sizes and non-spherical irregular shapes, the different refractive index and low degree of common alignment of the debris particles. (Ryzhkov, 2005)

The signatures for debris tracking just described are well detectable for large and strong tornadoes, as in these cases generally many debris are picked up. Therefore this type of tornado detection is very useful for monitoring the (more exact) tornado track, perform studies on how weather radars can become a significant warning mechanism and to keep statistics. However, this technique may be less valuable when it comes to using it as an early warning signal as the

signatures are only present when the tornado already has hit the ground and has done damage already.

When a tornado is small, there might not be any of these signatures present. This can be due to the fact of lack of the presence of large amounts of debris the short tornado life-span or because the radar resolution in either time or space or both is not sensitive enough to observe distinctive debris features.

Extensive literature is available describing tornado debris sampled by polarimetric radars, (Ryzhkov, 2005) (Kumjian & Ryzhkov, 2008) (Van Den Broeke, 2014), amongst others.

Wind shear A tornado itself rotates, meaning that when looking from the radar location to the tornado along its line of sight, it can be observed that one part of the fennel is rotating towards the radar while the other parts is moving away from the radar. This wind shear can be very well observed on the Doppler velocity scan of a weather radar; the radial velocity due to tornadic forcing is indicated with positive (wind towards the radar) and negative values (wind away from the radar) resulting in a couplet (contrasting colors indicating positive and negative velocities side by side). An example of wind shear due to a tornado is given in figure 3.8.

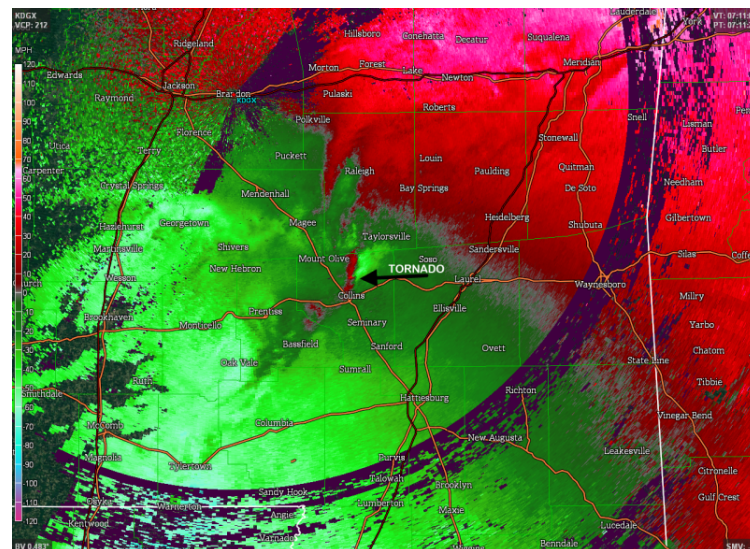


Figure 3.8: Mean Doppler radial velocity image from South-Central Mississippi captured on April 7th 2014. The wind shear is clearly present, indicated by the strong color transition from red (positive velocities) to green (negative velocities). The width of the tornado itself was around 540 meter.

When observing Doppler velocity outputs, attention should be paid to the possibility of velocity wrapping. In order to make sure that the image is not wrapped, two checks can be performed. A first sign of no-wrapping is indicated when a Doppler velocity gradient is present in the area of wind shear; in case of aliasing, the velocity values are expected to jump abruptly from one side of the spectrum to the other which is mostly a positive to negative value jump. Secondly, a (visual) inspection should be performed whether the velocities are higher or lower than the Nyquist velocity. When this is the case, indeed aliasing has occurred and the Doppler velocities need correction.

Spectrum width As last tornado radar signature, the spectrum width is addressed. Explained in chapter 2, spectrum width is a measure of velocity dispersion. Thus in a way a

verification method whether indeed high velocity changes or turbulence is present in a certain area.

Within the tornado itself large turbulence and wind shear are present, resulting in a big variability of Doppler velocity estimates. This means that when inspecting the spectrum width of a passing tornado, high values are expected to be found at the location of the tornado itself and lower values in its direct surrounding. An example of high spectrum next to Doppler velocity is given in figure 3.9.

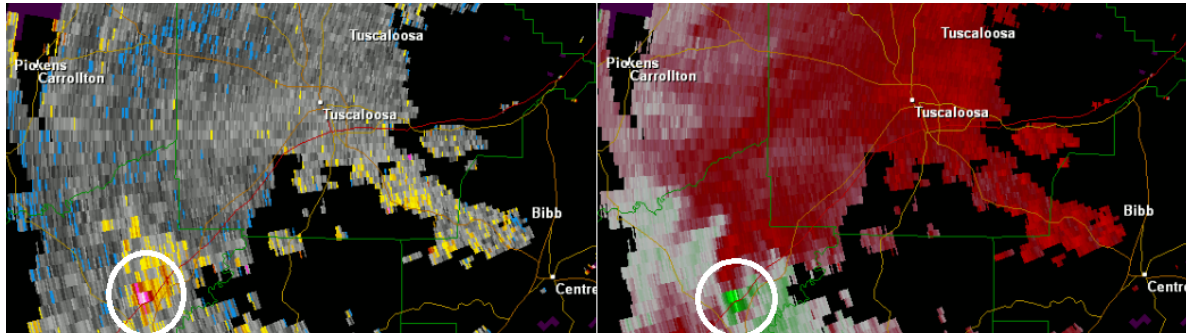


Figure 3.9: Spectrum width (left) and the Doppler velocity (right) of a super cell captured on December 16, 2000 in Tuscaloosa, the United States. The pink and white shaded area within the white circle is associated with high spectrum width values due to turbulent flow associated with circulation. On the Doppler velocity image, again, a velocity couplet is visible, where green indicates negative velocities and red positive velocities. Image adapted from: <http://www.spc.noaa.gov/>

Case Study & Data Set

In this chapter first the selected case date and the tornado touchdown time is presented followed by weather predictions and issued warnings on the day of the case. After this the trail of the rotating cell and reported damage by the tornado is described. Subsequently, the data sets obtained from the measurement systems during the case and the measurement devices itself are elaborated on.

4.1 Case date and touch down time verification

From cases described in Chapter 1, Table 1.1, the tornado event on the **3rd of November 2013** is selected to be used as a case study. The main motivation for the selection of this case is the location of tornado, as the trail of the rotating cell crosses the field of view of the high resolution X-band radar IDRA and thus also passes the atmospheric measurement site at Cabauw, CESAR. Next to this, the rotating cell is also within close proximity of the C-band radar at De Bilt which is operated by the Royal Netherlands Meteorological Institute.

Directly after the date was selected a detailed search for more information on the event was conducted. The main goal of this search was mainly to find an exact indication of the touchdown time of the tornado. From the preliminary search it is already known that the location of the touchdown was at a street called 'Broekweg' at the Dutch town Wijk bij Duurstede.

As news reports on the event did not provide any specific touchdown time information, an advanced search on twitter was conducted, for twitter is known for almost real time reporting by its users.

Subsequently, the first twitter report which appeared online at, 14:13 UTC, 15:13h local time, was confirmed by an article from the KNMI featuring a screen shot of the KNMI C-band radar reflectivity output which features a hook echo, a distinctive tornadic signature (KNMI, 2013). In figure 4.1, both the first twitter report on the tornado and the KNMI screenshots are presented.

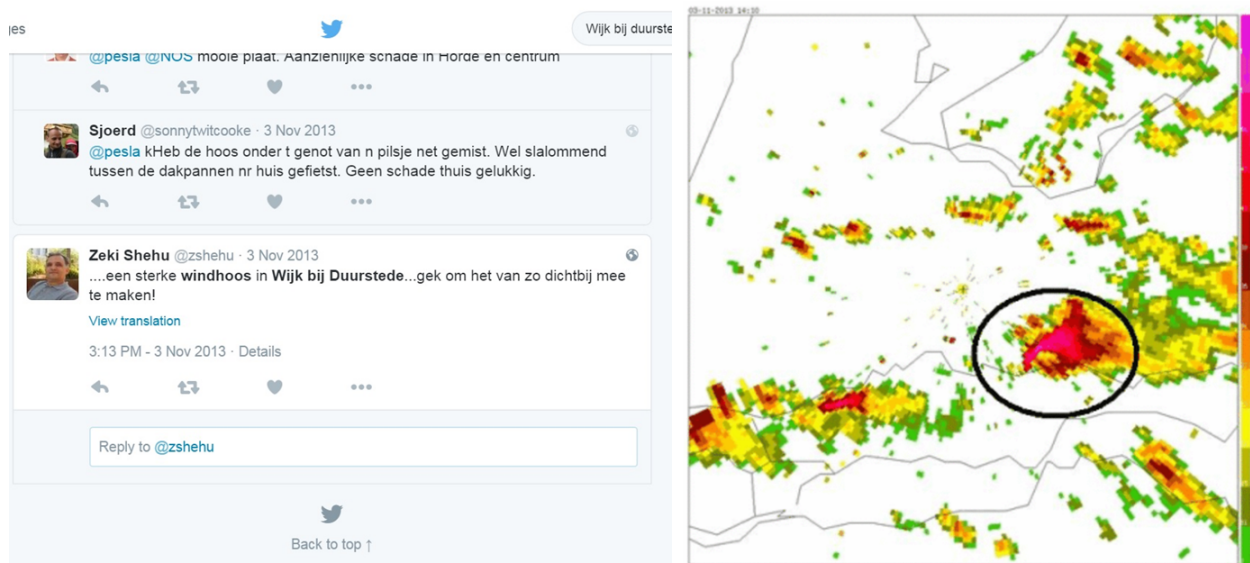


Figure 4.1: The first twitter message reporting about the tornado at Wijk bij Duurstede at 14:13 UTC (left) next to the released KNMI screenshot of the reflectivity by De Bilt (cross) taken at 14:10 UTC. The hook-echo is encircled and clearly visible in red.

4.2 Weather predictions and issued warnings

On the 8 PM news from the Dutch Broadcast Foundation (NOS) of the 2nd of November 2013, locally heavy precipitation accompanied by thunderstorms with strong winds, ranging from 5 Beaufort (8-11 m/s) inland to 7 (14-17 m/s) at the coast were forecasted. However, no warning or prediction on potential whirlwinds or tornadoes were mentioned (NOS, 2013b).

Next to news reports such as the 8 PM NOS news a surface pressure chart issued by the KNMI, presented in figure 4.2 was available. A low pressure area right above the United Kingdom can be well observed. This low pressure area indicates an active depression circulating above the North Sea. Due to this low pressure area a trench was progressing towards the Netherlands containing very cold air in the upper layers, causing a squally situation.

At 10:30 local time in the morning of 03-11-2013, the KNMI issued a 'code yellow' weather warning for thunderstorms only, effective from 12:00-18:00 local time. This was the official and only warning issued that day and which was continually repeated on the news.

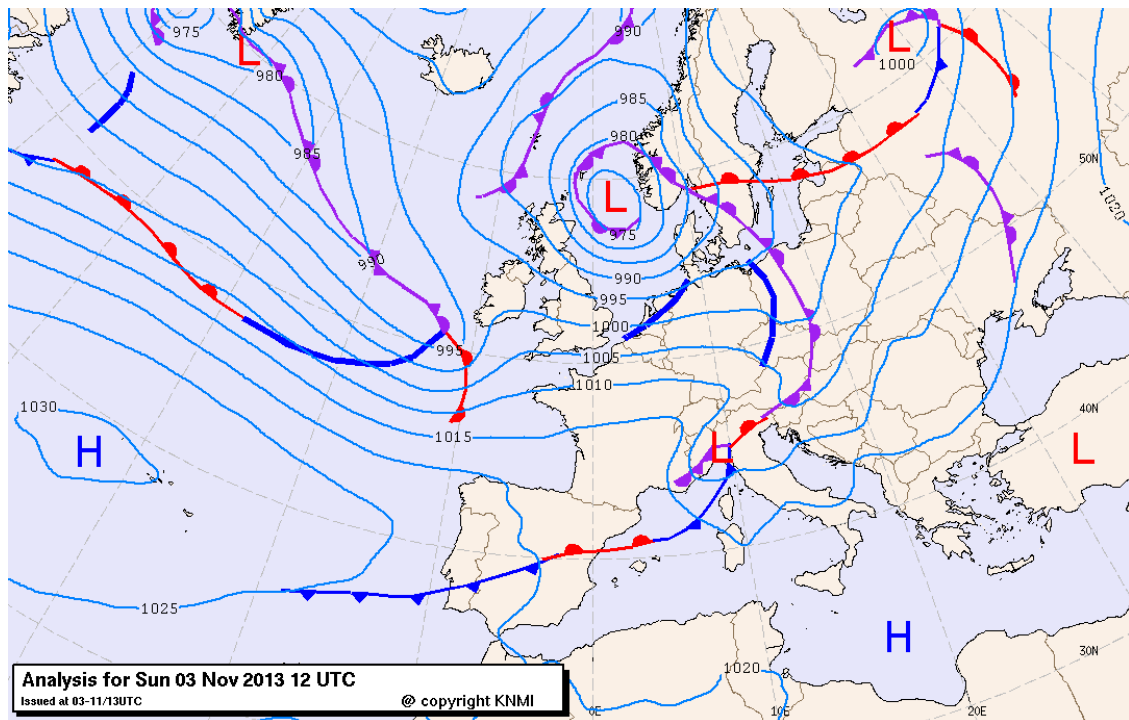


Figure 4.2: Surface pressure chart of 03-11-2013, issued by KNMI, strong wind and thunderstorm are expected due to the cold front at the border of the Netherlands

4.3 Reported trail of rotating cell and proof and damage by the tornado

On the 3rd of November 2013, in the afternoon, from several locations in the middle of the Netherlands, near Utrecht a strong whirlwind was observed.

Around 14:00 o'clock local time, a local depression started to develop into a strong cell between the cities Schoonhoven and Vianen, in the province Zuid-Holland (KNMI, 2013). Within 15 minutes, medium showers developed into a cloudburst. The cloud deck, turned very dark and featured heavy rain, also hail precipitation is reported (van der Kolk, 2013).

Based on eyewitness reports, the rotating cell with occasionally a beginning tornado fennel appearing started developing at approximately Schoonhoven (balloon 1), another preliminary fennel was then spotted at Vianen (balloon 2), then one at Everdingen (Balloon 3) and finally one at Wijk bij Duurstede (ballon 4) where the dynamics where is such condition for the fennel to make a touch down. In figure 4.3 the path of the rotating cell is presented on a geographical map as reported by eye witnesses (van der Kolk, 2013).

At Wijk bij Duurstede the rotating cell developed a tornado which had its touch down at an industrial site of the city at 14:10 UTC. After damage examination, it was determined that the tornado reached wind speeds between 140 to 150 kilometers an hour and that it had a damage path of 2 kilometers long and 60 meters wide while the tornado lasted for just 2 minutes (van Nederland, 2013). This means that the tornado reached EF1 on the Enhanced Fujita scale Ladue & Mahoney (2006), a scale that rates the strength of tornadoes based on the damage they cause. EF1 strength corresponds to wind speeds between 3849 m/s (138-178km/h), a rare event in the Netherlands.

Proof of the tornado and its development is presented in figure 4.4. In figure 4.5 shots from multiple locations of the same tornado are shown when it is at its peak strength.

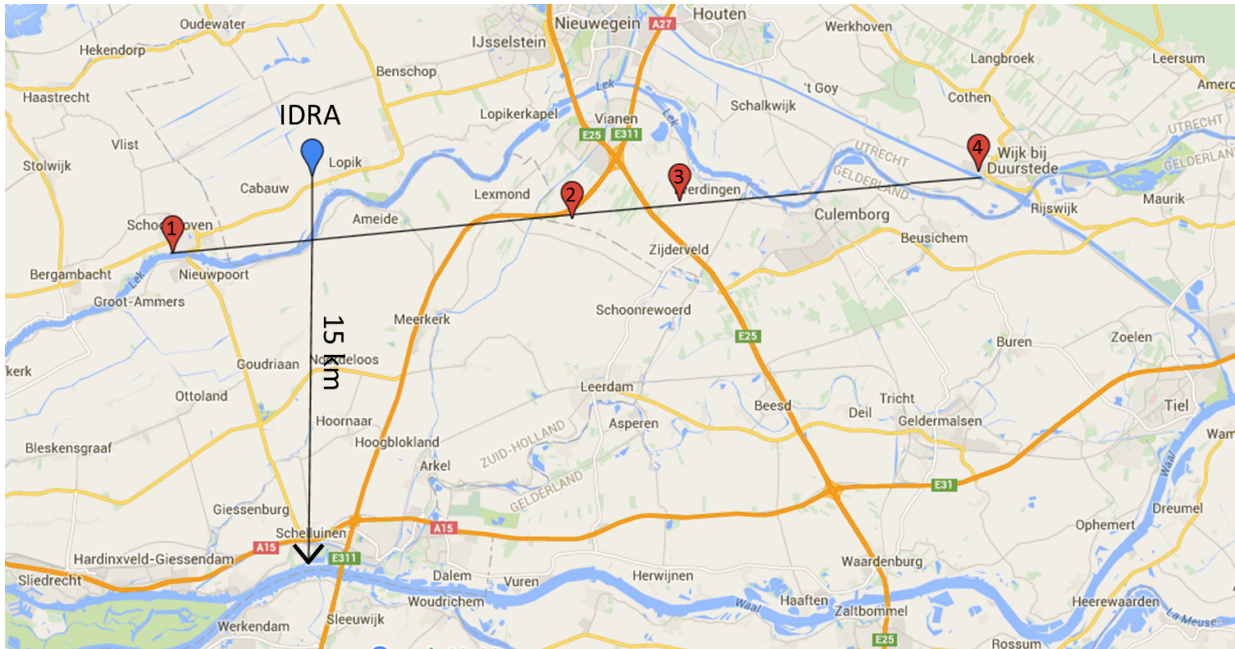


Figure 4.3: Reconstructed path of the rotating cell, the red numbered balloons represent locations confirmed by eyewitness reports.

The damage caused by the tornado featured unstable buildings, wrecked roofs (missing roof tiles, destroyed facades, leakages, etc.), shattered windows, damaged cars (partly due to uprooted trees) and many snapped lanterns (dangerous due to electrocution risks). The total damage cost entailed several millions of Euros. No fatalities or injuries were reported that day, though it must be noted that the tornado took place on a Sunday afternoon at an industrial area.

Pictures of the damage can be found in figure 4.6.



Figure 4.4: Development of the Tornado at Wijk bij Duurstede as seen from the Dutch city Houten, approximately 15 km away from Wijk bij Duurstede. Pictures taken between 14:09-14:15 UTC. Source: twitter.



Figure 4.5: Tornado at Wijk bij Duurstede, shot from several locations around it. Source: Twitter



Figure 4.6: Damage after the touch down of the tornado at the industrial area 'Broekweg' at Wijk bij Duurstede. Source: Twitter

4.4 Data acquisition & Measurement instruments

In this section all measurements systems used in this report are presented. Many of the measurement systems used are located at one site, Cabauw Experimental Site for Atmospheric Research (CESAR) observatory. The reason for this is because the area of interest of this case study lies within the boundaries of this observatory.

The CESAR observatory operated by the Royal Netherlands Meteorological Institute (KNMI) is located in the center of The Netherlands between the villages of Cabauw and Lopik (51.971 °N, 4.927 °E). CESAR is a collaboration between three Dutch Universities: Universiteit Utrecht, Delft University of Technology and Wageningen University and Research Centre and 5 major research institutes. It has several high resolution measurement systems on site installed of which the collected data is stored in a freely accessible database, that can be found on <http://www.cesar-database.nl>. In figure 4.7 the layout of the site with its instruments is presented (Leijnse, 2010). A Present Weather Station (PWS) is indicated in this figure as well, as this device is not used in this report it will not be further mentioned.

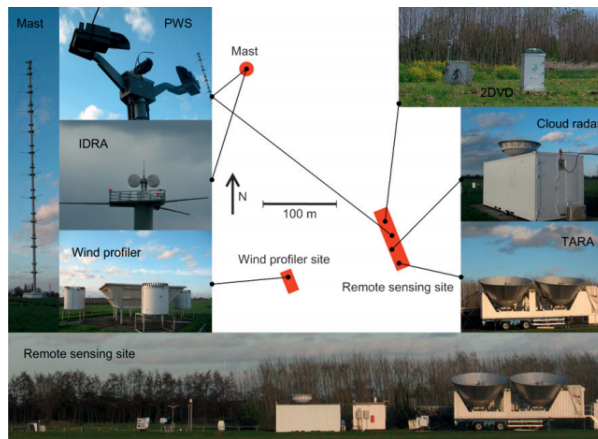


Figure 4.7: Schematic drawing of the CESAR site layout, with locations and photographs of the different instruments discussed in this paper (photograph of IDRA is by Raymond Shaw and all others are by Hidde Leijnse).

In table 4.1 a list of the measurement systems and its technical specifications used for the analysis of the tornadic event is shown. Specific information on data storage and main operator can be found in the following sections where each measurement system is individually addressed.

Table 4.1: Measurement system configuration and technical specifications used on 03-11-2013

Measurement system	Temporal resolution	Range resolution [m]	Max range [km]	beam elevation [°]	Polarization	Band
IDRA	1 [min]	30	15	0,5	Dual	X
TARA	1.5 [s]	30	14.64	45	Dual	S
35GHz CloudRadar	15 [s]	89	13	90	Dual	L
Wind Profiler	5 [min]	60	check	90	n/a	n/a
in-situ tower	10 [min]	n/a	0.213	n/a	n/a	n/a
C-band radar	5 [min]	1000	200	0.3-25	Horizontal	C

4.4.1 IDRA, X-band radar

On top of the observatory mast at a height of 213 meter IDRA is installed, a frequency-modulated continuous-wave (FM-CW) dual-polarized X-band Doppler radar (Figueras I Ventura, 2009). IDRA operates at X-band wavelength: 3 cm and is classified as a high resolution radar with a spatial resolution of 30 meters. The total effective range of IDRA is 15 km. IDRA has a scan velocity of 1 rpm clockwise, which means a temporal resolution of one minute, at a set elevation angle of 0.5 degrees, as shown in figure 4.8.

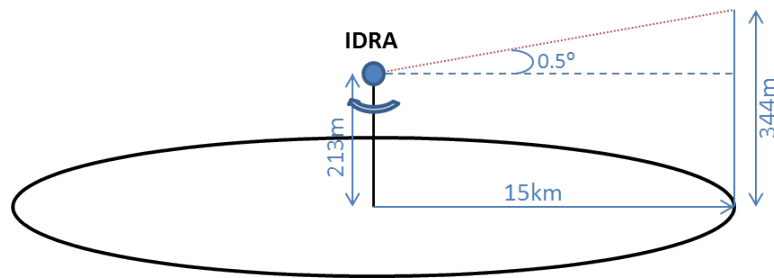


Figure 4.8: Schematic drawing of IDRA, the red dotted line illustrates its radar beam and the solid black circle are the outer bounds of its range of view. The radar rotates clockwise with an elevation of 0.5 degrees above the horizon.

In order to suppress clutter and to enhance precipitation correction, spectral polarimetry is applied in real-time data processing Unal (2009). IDRA data is available via the 3TU data base (<http://datacentrum.3tu.nl/>) and via the cesar-database. IDRA has the same output parameters as presented in table 2.4, except the specific differential phase K_{dp} .

Missing and unusable IDRA data Due to technical difficulties during the day of the case, only data recorded between 13:38-13:49 UTC is available. Next to missing data in time, also radial data is missing due to problems with the data collection algorithm. Unfortunately, nothing can be done to retrieve this information. Nonetheless, the available data results in a strong case and is worth describing.

Next to missing data, also the data quality of IDRA's polarimetric outputs are affected. After visual inspection of the depolarization parameters, it is found that the linear depolarization ratio (L_{dr}) and differential reflectivity (Z_{dr}) recorded during the time of the case study are strongly inaccurate.

Typical L_{dr} values of a rain medium, recorded by an X-band radar, range between -12 and -30 dB and mostly remain smaller than -25 dB (Iguchi, 1992). L_{dr} values recorded during the pass by of the tornado are mainly between -10 and -12 dB with peak values around -17 at the center of the storm.

Next to unreliable L_{dr} values, also unreliable Z_{dr} values were observed. From (Doviak & Zrnica, 2006), it is adapted that in cases of moderate to heavy rain differential reflectivity values between 0.5-4 dB are reached for X-band radars, while hail and graupel generally have Z_{dr} values between -2 and 0.5 dB.

During the time interval of interest, the horizontal reflectivity scan indicates areas of heavy and moderate precipitation which are verified with the KNMI C-band radar. However, the values found in the Z_{dr} scans do not comply with it. Instead of positive values between 0.5 and 4 dB, negative values around -2 are observed from the data. This means that by solely observing the unreliable differential reflectivity data, the conclusion was that hail or graupel should be present not in but all around the center of the storm, which is a very unlikely scenario.

4.4.2 TARA, S-band radar

TARA, (Transportable Atmospheric RADar) is located South-West to IDRA at the CESAR observatory. Similar as IDRA; it is a frequency-modulated continuous-wave (FM-CW) dual polarimetric radar, however it operates at S-band instead of X-band, thus has a larger wavelength. With one main beam and two side beams both pointing with an offset of 15 degrees, one in the horizontal and one in the vertical plane with respect to the main beam, TARA is able to provide vertical Doppler velocity and horizontal wind speed and direction at high temporal (3 seconds) resolution. All antennas are pointing at a fixed elevation which can be manually adjusted if desired, where the main beam is in this case set on 45 degrees elevation and 246.5 degrees azimuth, see figure 4.9 for a interpretation of this configuration. TARA has a spatial resolution equal to 30 meters and is able to provide observations up to 14640 meters upwards (Heijnen, 2000).

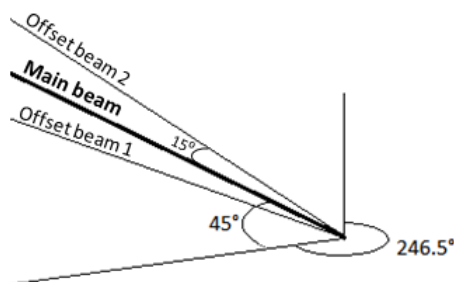


Figure 4.9: Schematic drawing of TARA, with a main beam elevation elevation of 45° above the horizon and 2 offsets beams. One with a 15° positive offset with respect to the main beam in the vertical plane and one at a 15° offset in the horizontal plane. All beams are directed South-West-West with an azimuthal angle of 246.5° for the main beam.

TARA has 4 primary output variables, which are displayed in table 4.2. Additional polarimetric outputs are not directly available in the database but can be obtained by request.

Table 4.2: Four direct outputs from TARA

Output	Description	Unit
Z_{hh}	co-polarized equivalent reflectivity factor at horizontal polarization	dBZ
V_z	vertical mean Doppler velocity	m/s
V_h	Horizontal wind speed	m/s
D	Horizontal wind direction	deg

De-aliasing horizontal wind measurement data of the case study Due to high levels of turbulence during the time of measurements on the 3rd of November, aliased velocities in the horizontal observations took place (see figure 4.10, the left image).

This phenomena can be corrected for by multiplying the aliased data by either minus or plus twice the Nyquist velocity (see section 2.6.1.2) which in this case was equal to 9.096 m/s. The result of the de-aliasing of the data is presented in the right image of figure 4.10.

4.4.3 Tower in-situ measurements

Next to radar measurements, in-situ measurements at the CESAR observatory are available from on ground and tower measurement systems.

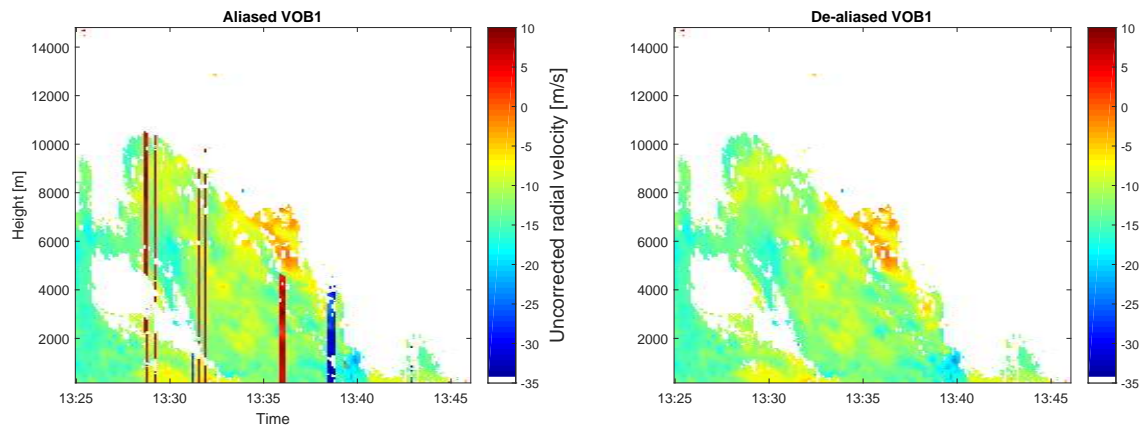


Figure 4.10: Left: aliased image of the first offset beam of TARA. Aliasing due to wrapping is clearly visible as the high positive velocity lines represented in yellow. Right: the de-aliased image of the first offset beam of TARA

At a temporal resolution of 10 minutes, on ground measurements of wind speed, wind direction, temperature, air pressure and precipitation measurements are obtained. The on ground wind measurements are taken at a reference height of 10 meter, while the temperature, pressure and precipitation are taken at 2 meter.

Tower measurements feature only wind speed, wind direction and temperature. The tower profile entails seven reference heights at which observations are taken: 2, 10, 20, 40, 80, 140 and 200 meter. The data used in this report is already gap filled by the climatological service of KNMI (M. & Bosveld, 1997).

4.4.4 Windprofiler

The LAP3000 1290 MHz pulsed Doppler windprofiler is located approximately 300 meter South of the IDRA mast. The profiler has a short pulse and a long pulse mode which are continuously alternated. The short pulse has a maximum range of 2000 meter and high range resolution, of 58 meters while the long pulse has a maximum range of 7000 meters a low range resolution of 202 meter. The phase controlled antenna performs measurements with 5 different angles, one vertically and 4 off-zenith with an elevation of 74.5 degrees above the horizon. The wind profiles are reconstructed over a time interval of 30 minutes by combining the radial velocity of the off-set measurements of the antenna. During this reconstruction it is assumed that each measurement bin has a stationary atmosphere and that within one bin a more or less homogeneous wind vector field is present.

For this case study, only the short pulse data is used. The first reason is because its significant higher resolution interesting signatures are better observable than from the long pulsed data, the second reason is because the most interesting part of a tornado is near the ground.

4.4.5 Cloud radar

The 35GHz Doppler Cloud radar located next to TARA at the CESAR observatory is permanently aimed at a 90 degrees elevation. The radar has a range resolution of 89 meters, a temporal resolution of 15 seconds and a maximum range of 13 km in the vertical direction. Due to its

high frequency, as this radar is designed to measure cloud base heights which mainly consist of small droplets, this radar is very sensitive to signal attenuation due to precipitation.

To give a better understanding of this idea: cloud droplets are typically 15 micron but can range between 1-100 micron of diameter. Raindrops are 10-1000 times bigger than cloud droplets and have a typical diameter of 2 mm. Since raindrops are of the same order of magnitude with respect to the wavelength of this radar, signal attenuation occurs easily.

4.4.6 KNMI's C-band radars

The current operational Dutch weather radar network consists of two identical SELEX Meteor 360 ACC C-band Doppler radars, one located at De Bilt and one at Den Helder (see figure 4.11). Both radars have a range of 200 km and operate at a temporal resolution of 5 minutes and a spatial resolution of 1 kilometer. A 14-elevation scan volume is generated with scans from the following elevations: 0.3°, 0.4°, 0.8°, 1.1°, 2°, 3°, 4.5°, 6°, 8°, 10°, 12°, 15°, 20°, 25°. The KNMI has put three types of data available for public use:

- Output parameters per volume scan of De Bilt
- Output parameters per volume scan of Den Helder
- Reflectivity of radar composites of De Bilt and De Helder scans

With output parameters per volume scan is meant all parameters which a single polarized Doppler radar produces are per volume scan available.

Reflectivities of the composite scan are based on a combination of scans of the elevation 0.3, 1.1, 2.0 and 3.0. Per radar, first a single image is constructed by linearly interpolating reflectivities in altitude, while a constant height of 1500 meter is kept. Subsequently, the two radar images are combined to one, by taking the weighted averages of the reflectivities. All data is processed and available at the KNMI Data Centre (KDC). KNM (n.d.)

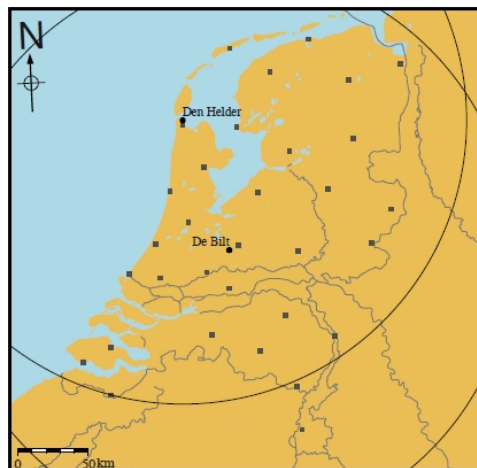


Figure 4.11: KNMI C-band radar coverage of the Netherlands, the two circles represent the maximum range of each radar and the black squares the locations of other KNMI weather stations

Analysis of high resolution X-band IDRA data

In this chapter IDRA recorded data of the passing of a rotating cell is analyzed and presented. As the linear depolarization ratio and the differential reflectivity are too unreliable to present, attention is paid to the four remaining interesting parameters: co-polarized horizontal reflectivity, Doppler radial velocity, Doppler spectrum width and the specific differential phase. For IDRA data it is common to correct reflectivity scans for attenuation with use of specific differential phase data. However, since the quality of the specific differential phase data is uncertain the attenuated reflectivity scans are presented.

For analysis of the reflectivity, specific differential phase, Doppler velocity and spectrum width, scan times 13:42, 13:45 and 13:49 UTC are selected, as these times show the most significant features and have the most complete data set with respect to radial data.

First wind shear signatures which are found on the radial Doppler velocity scans, are presented and verified with its corresponding spectrum width. After this tornadic cell signatures such as the v-notch and hook echo are presented followed by a reconstruction of the touch down time, obtained with use of the IDRA wind shear observations. Lastly, findings of the specific differential phase and the reflectivity scans are presented.

5.1 Wind shear signatures verified by spectrum width

Before analyzing the Doppler velocity data from IDRA, first it should be checked for aliased velocities. This can be done by verifying whether the Doppler velocity values in the dataset are higher or lower than the radar specific Nyquist velocity. In order to perform this check, IDRA's Nyquist velocity (V_{max}) should be obtained, which can be done with the following formula:

$$V_{max} = \pm \frac{\lambda}{4T_s} \quad (5.1)$$

Given that the wavelength of IDRA is equal to 3.164 cm and the sweep time (T_s) is equal to 409.6 μ seconds, the Nyquist velocity of IDRA is 19.31 meters per second. This is higher than the maximum speeds within the dataset of the case study which leads to the conclusion that no aliasing is present.

When inspecting the radial velocity data, a consistency in high wind shear that moves from West to East on the radar is observed. These high wind shear signatures are assumed to represent the rotating cell from which later on the tornado at Wijk bij Duurstede develops.

Radial Doppler velocity alongside its spectrum width of the time interval 13:42, 13:45 and 13:49 UTC is presented below in figure 5.1 to show this high wind shear. Velocity contours are constructed around the wind shear pixels in order to make the interesting signatures easy distinguishable. The high spectrum width within the velocity contours (presented black) supports the theory that within these contours the rotating cell is located as these high values indicate high turbulence and large changes in velocity; these shapes indicate the rotation of the wallcloud. The dimensions of these shapes remain rather consistent over time and have measurements of approximately 700x700 meters.

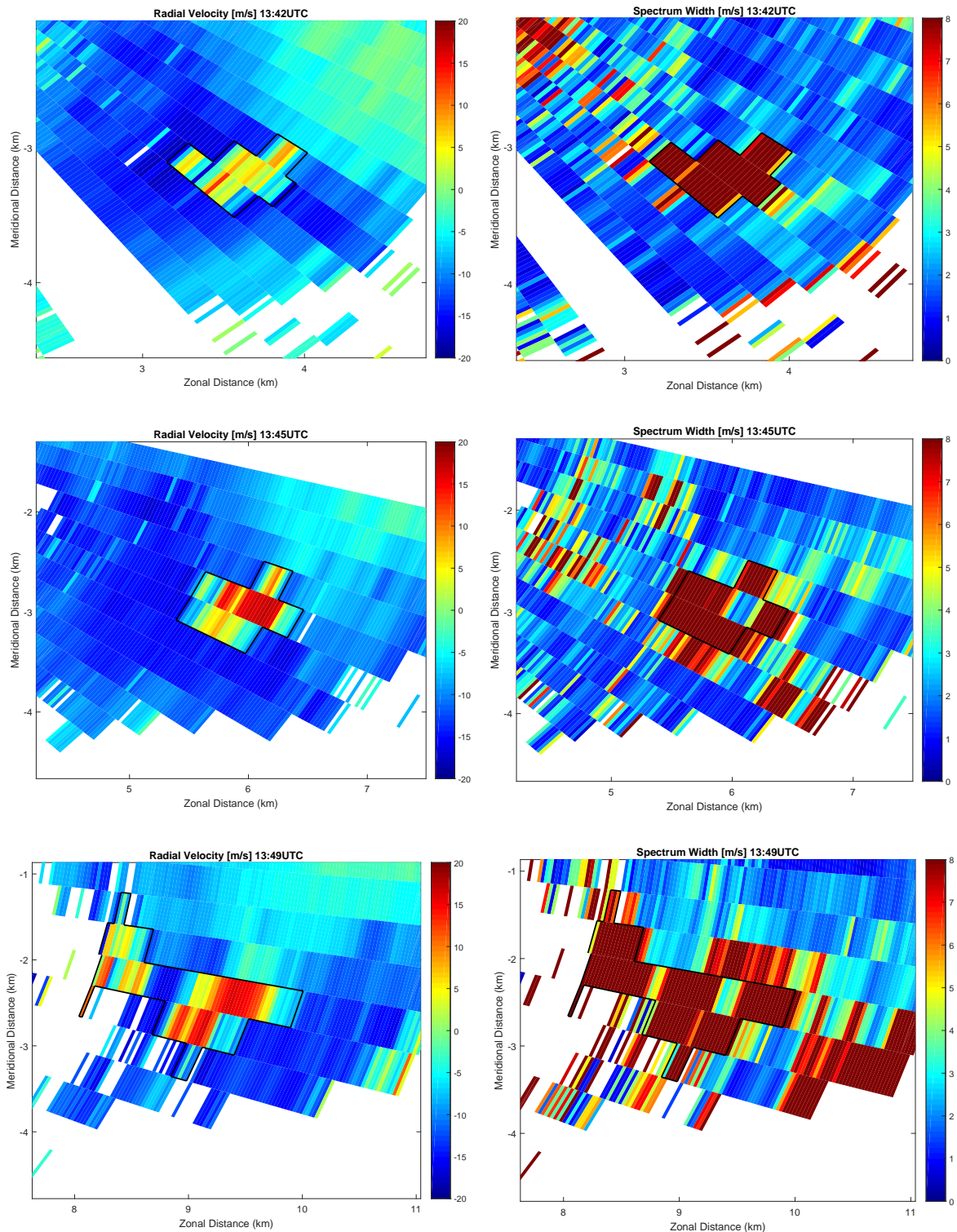


Figure 5.1: Partly zoomed PPI of IDRA, all left images represent the radial velocity, while all right images are the spectrum width, at times 13:42, 13:45 and 13:49 UTC from top-down. A black contour is applied to indicate the interesting areas of wind shear.

5.2 V-notch and hook echo

In figure 5.2, the IDRA PPI on a partly zoomed reflectivity is presented. A straight line is laid over the reflectivity in order to indicate the assumed ground track of the rotating cell. Note: this ground track is based on eyewitness reports, so it may not be completely accurate. In magenta, wind shear pixels are highlighted which can be distinguished from the radial Doppler velocity data. In all images the v-notch signature is clearly present and indicated with black v shaped lines. In the snapshot taken at 13:49 UTC the hook echo is indicated by the arrow.

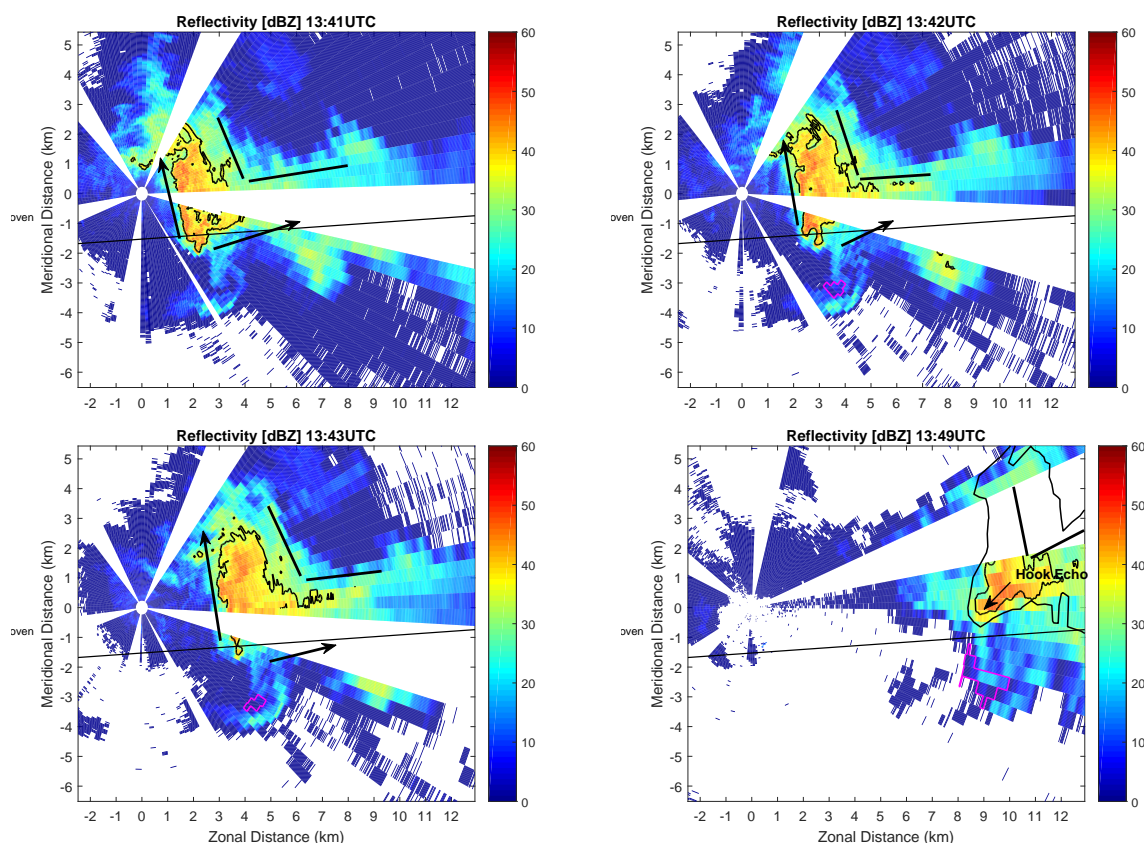


Figure 5.2: Partly zoomed reflectivity PPI of IDRA, the straight black line represents the assumed trail of the rotating cell. A reflectivity contour is applied at a cut-off of +35 dBZ, the additional black contour line at 13:39 represents the 35 dBZ contour of the KNMI C-band radar at its corresponding time. The magenta colored block formed shape South of the assumed trail represents high wind shear pixels and the black v shaped lines indicate the v-notch.

5.3 Reconstruction of the touch down time

With IDRA every minute a scan is taken and from visual inspection on figure 5.3 the wind shear signature remains very well traceable between the time interval 13:42-13:49. By tracking the progression speed of the rotating cell its average progression speed can be reconstructed and as well as its theoretical touch down time based on this found average progressing speed. First, with use of these wind shear pixels the distance traveled by the tornado per scan, thus per minute can be computed, see table 5.1. Subsequently, the speed per minute can be computed and from this an average progression speed can be found.

Table 5.1: Distance traveled and ground speed of the rotating cell based on the movement of IDRA wind shear pixels per 1 minute time interval. The average speed of the tornado is equal 14.5 m/s based on 7 data points.

Time interval UTC	Distance traveled [m]	Equivalent speed [m/s]
13:42-13:43	806	13,4
13:43-13:44	922	15,4
13:44-13:45	912	15,2
13:45-13:46	802	13,4
13:46-13:47	856	14,3
13:47-13:48	850	14,2
13:38-13:39	962	16,0

During this analysis it is assumed that the rotating cell is following the path presented in figure 4.3, thus maintaining a straight line. It is also assumed that the estimated ground speed obtained with use of the wind shear pixels remains constant as by inspection of the feed data, no significant outliers are present.

Now in order to reconstruct the touchdown time, the distance where the wind shear is at 13:42 UTC from the actual touch down location (23.5 km) should be divided by the average speed based on the wind shear pixel progression.

Thus by dividing 23.5 kilometers by the average tornado speed of 14.5 m/s, a theoretical travel time of 27 minutes exactly is found for the rotating cell to reach Wijk bij Duurstede. This means that from this reconstruction the rotating cell should reach Wijk bij Duurstede at (13:42 UTC + 27 minutes) 14:09 UTC which is 1 minute earlier than the reported actual touchdown time of the tornado that developed from this rotating cell: 14:10 UTC.

In figure 5.3, the full available data set of the radial velocity data including the wind shear pixels indicated by a black contour is presented.

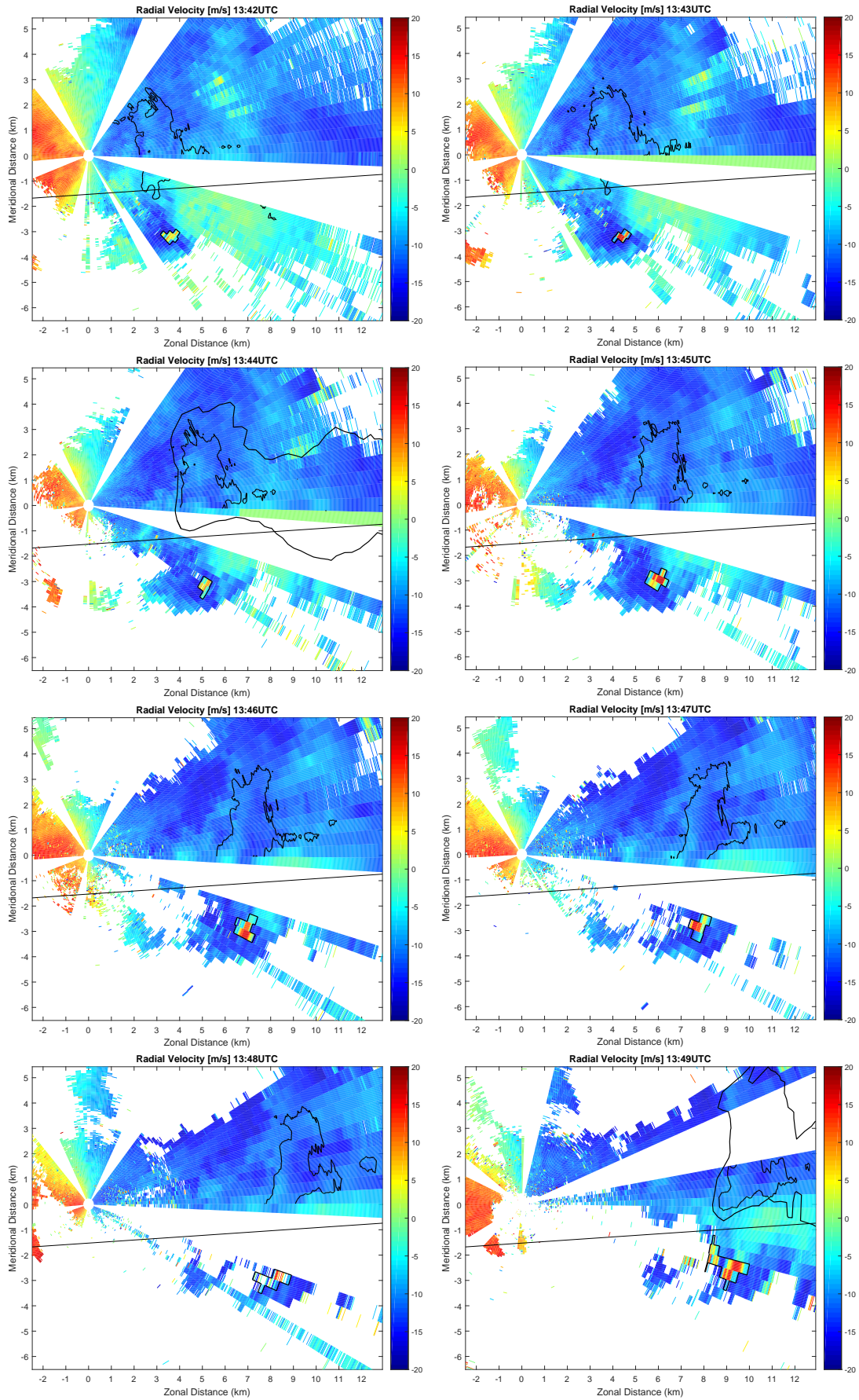


Figure 5.3: Full data set of the partly zoomed in radial velocity data including the wind shear pixels highlighted by a black contour. The almost horizontal line represents the reported trail of the rotating cell.

5.4 Specific differential phase

Explained earlier, the specific differential phase is a valuable but difficult parameter as it becomes noisy very fast. It is only reliable where reflectivity values above 25 dBZ are found and where enough data along the radial is present.

In figure 5.4 two specific differential phase and reflectivity images are presented side by side for the most interesting time scan of this case.

Because of the dependency of differential reflectivity, which was stated to be unreliable, there is a significant uncertainty whether the obtained specific differential phase data is reliable or not. However, when analyzing the area within the 35 dBZ contour, at the tip of the hook, expected high values for the specific differential phase are found. Also there is enough information available along the radial in order to construct good K_{dp} results.

In theory it means that very heavy rain is present there, which is in line with the reflectivity values found on the reflectivity scan at that location. Very heavy precipitation in close proximity of a rotating cell with tornadic features is a common phenomena, which is the reason why this images is presented.

Due to low reflectivity values near the wind shear area, the specific differential phase at this area will not be discussed as it is considered noisy and unreliable.

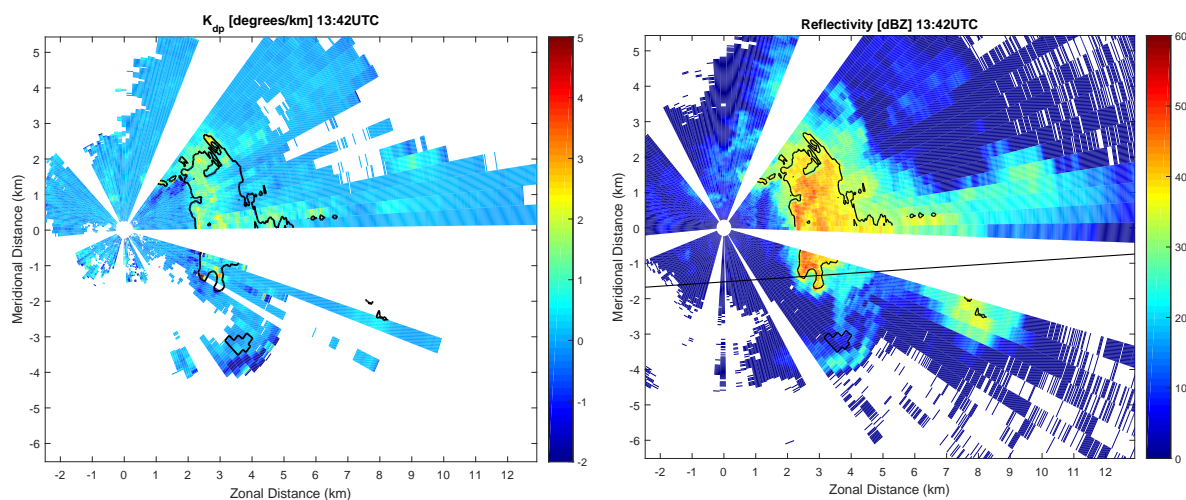


Figure 5.4: Partly zoomed PPI of IDRA, the left image represents the specific differential phase, while the right image is the attenuation corrected reflectivity based on the specific differential phase, at 13:42 UTC. The straight black line on the right image represents the assumed trail of the rotating cell. A contour is applied at a reflectivity cut-off of +35 dBZ. The black block formed shape South of the assumed trail represents high wind shear pixels.

Case verification with use of additional data sets

In this chapter, the rotating cell passing Cabauw on 03-11-2013 is verified with other available measurement systems. First KNMI C-band radar scans are analyzed. This is followed by results from TARA and the in-situ profile measurements from the CESAR tower. Subsequently, the KNMI CloudRadar and Wind Profiler observations are presented and discussed.

6.1 KNMI C-band Radar

As explained in chapter 4, the weather situation during the day of the case was unstable. Strong winds were present and the KNMI gave out a code yellow weather alarm for thunderstorms throughout the country. At 14:10 UTC a tornado had its touchdown at Wijk bij Duurstede.

From the KNMI data center, C-band radar output parameters per scan elevation, per measurement stations and of the total composite scans are freely available. Therefore, both scans recorded around the touchdown time are used to verify the tornado case.

One day after the tornado event, the KNMI published 'proof' of the most distinguished signature; they confirmed that a hook echo was spotted on the De Bilt C-band radar at 14:10 UTC (4.1, right image).

In order to verify whether the spotted hook echo observed by the KNMI is not a random signature, a composite scan of the next time interval, 14:15 is constructed to proof consistency.

In figure 6.1, a KNMI C-band radar composite scan over the Netherlands is presented at 14:15 UTC on the 3rd of November 2013. When inspecting the images, a straight line of strong precipitation can be observed, starting from Rotterdam and reaching to the East, into Germany. When zooming in, this snapshot features both the famous hook echo as well as the V-notch signature, an indication of a storm cell passing with tornadic features.

In order to perform a check whether the KNMI's reported tornadic signatures are related to the found wind shear by IDRA, a visualization is created which fits IDRA's wind shear pixels. For this visualization the second lowest elevation scan of De Bilt, 0.4 degrees is used, as the lowest elevation (0.3 degrees) is corrupted by clutter. The reason for the selection of a low elevation angle at De Bilt is because the scan heights of both IDRA and De Bilt are then at approximately the same elevation, such that their outputs are comparable.

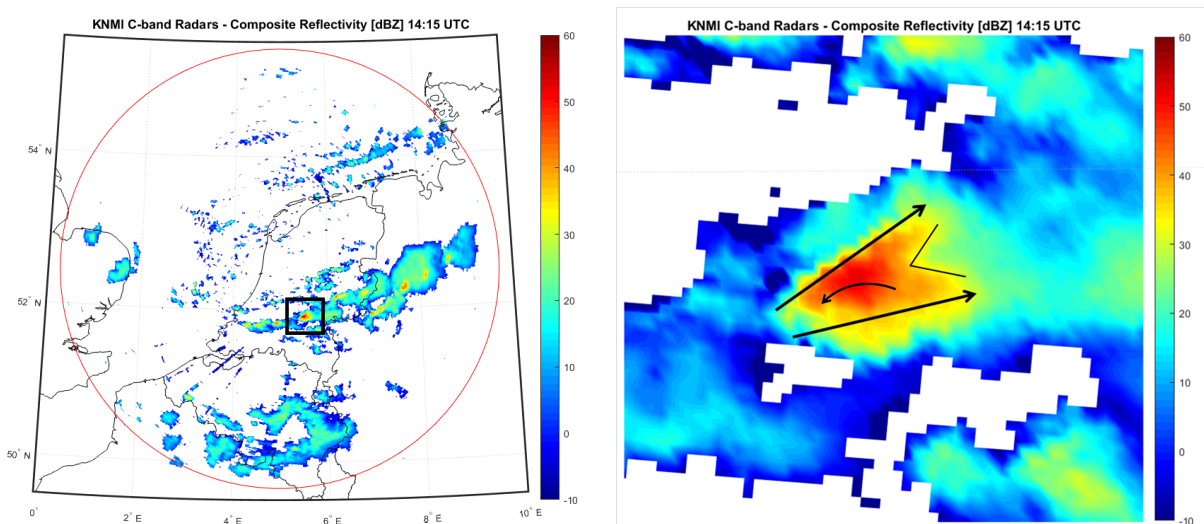


Figure 6.1: Composite C-band radar snapshot, left is the representation of the complete composite reflectivity scan. The red circle represent the theoretical reach of the composite scan. Right, the zoomed-in square found in the left image is shown. The black straight arrows are added to illustrate the V-notch of cell, which features the hook echo signature within.

The wind shear recorded by IDRA starts to become clearly visible between 13:42 and 13:49 UTC, approximately 20-25 minutes prior to the touchdown of the tornado at 14:10 UTC. By visual analysis it is established that IDRA data of time interval $[t-1\text{min} - t]$, where t is the scan time of the KNMI De Bilt C-band radar, fits well with the C-band radar data. This means that in the C-band reflectivity scan of 13:45 UTC, IDRA data of 13:44-13:45 should be overlaid. Due to the fact that the temporal resolution of the KNMI C-band radar is 5 minutes and the constraints due to the field of view and available data of IDRA, only two scans are suitable for presentation, the scan at 13:45 and 13:50 UTC.

From both top images of figure 6.2 where the reflectivity output of the C-band is laid-over by wind shear pixels recorded by IDRA, it can be established that the wind shear represented in white does match well with the shoulder of the hook echo. Especially at 13:50, the hook is well distinguishable. In both images the v-notch, shaped like the letter v is slightly stretched out but well distinguishable in red which indicates high reflectivities.

It is important to note that due to the low range (1000 m) and temporal resolution (5 min) of the KNMI C-band radar, it very likely that any high wind shear and spectrum width signatures induced by the rotating cell are smooth out over a few pixels, as from IDRA observations it is established that the dimension of this cell is 700x700 meter. This the reason why no distinctive signatures can be found on either one of these scans except for a large shape on the Doppler velocity images following the form of the 30 dBZ contour, which is mostly due to turbulence of the precipitation itself.

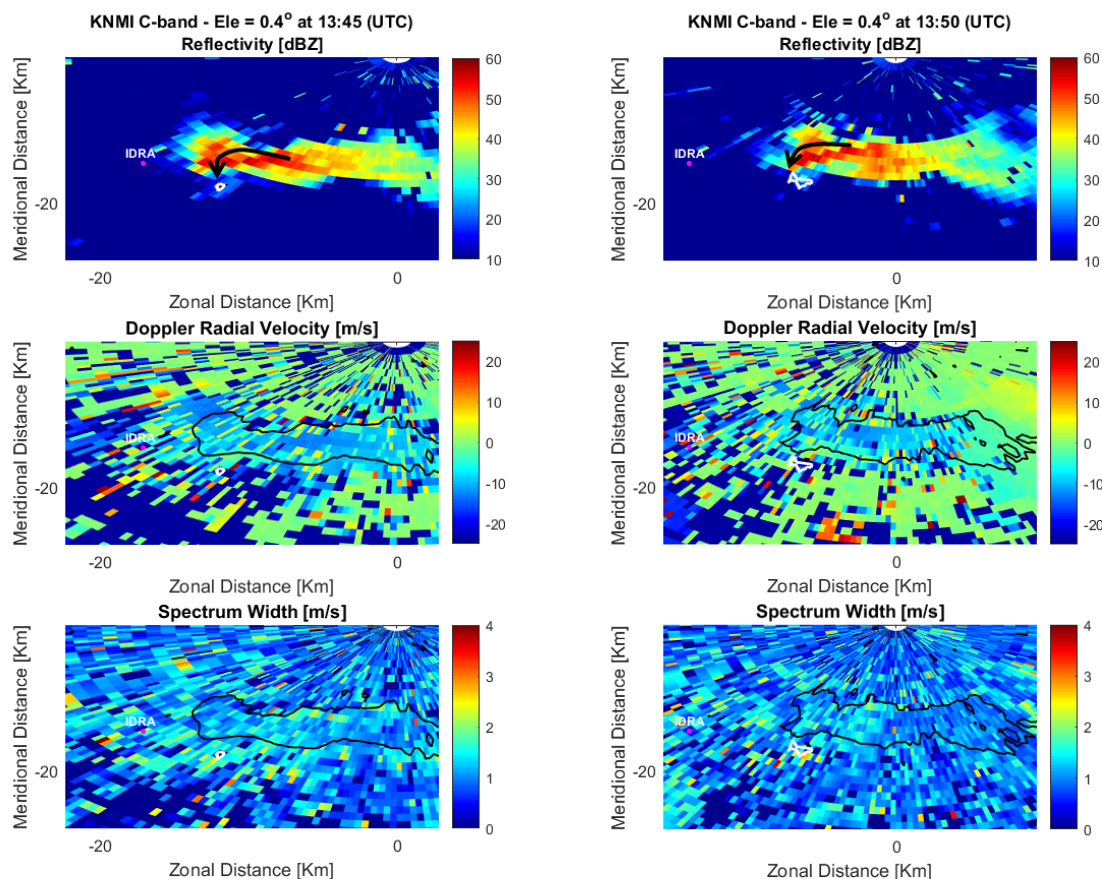


Figure 6.2: De Bilt C-band radar scan at a 0.4° elevation, presenting from top down: reflectivity, radial Doppler velocity and Spectrum width. The left side represents the scan taken at 13:45 UTC while the right side represent the 13:50 UTC scan. The location of IDRA is indicated with a magenta colored dot, the white shape at the shoulder of the hook echo is the IDRA wind shear contour. The black contour lines at the radial velocity and spectrum width indicate a reflectivity contour of 30+ dBZ of the De Bilt C-band radar.

6.2 TARA, S-band radar

In this section, two time intervals will be displayed. First the zoomed-out time interval, between 12:00 and 14:00 in order to discuss the overall storm dynamic and second the zoomed-in time interval to address the rotating cloud itself.

6.2.1 TARA - zoomed-out storm capture

Figure 6.3 shows a zoomed out reflectivity scan by TARA, at elevation of 45 degrees of the main beam. It is well visible that the rotating cell that produced a tornado at 14:10 UTC 25 km away at Wijk bij Duurstede, captured from 13:30 UTC to 13:42 UTC by TARA, is an isolated cell. At an elevation of 6000 meter at around 13:30 UTC, the cell slightly touches the preceding storm cell but as very low reflectivity is present at the boundaries, it can be assumed that no significant interaction between the two cells took place. The theory that the cell passing by between 13:30-13:42 UTC is isolated is supported by horizontal wind speed and direction

TARA data, as no wind speed and direction measurements are recorded at the location where the two cells are proceeding each other at TARA's line of sight while precipitation was present. These observations are not included in the report due to lack of significant relevance. Based on these findings, it can be assumed that an isolated rotating cell is passing Cabauw, which TARA recorded between 13:30-13:42 UTC.

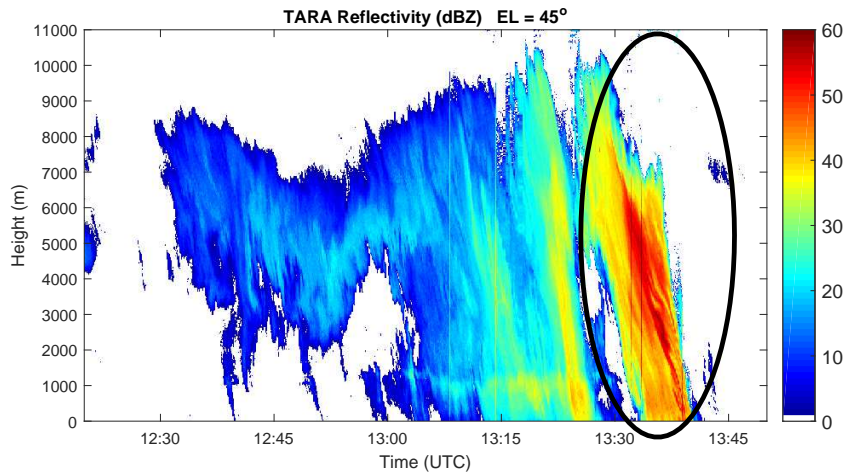


Figure 6.3: TARA reflectivity plot of the interval 12:20-13:50 UTC. In the time interval 13:30-13:42 UTC an isolated cell can be observed with very high reflectivities in the center.

6.2.2 TARA - zoomed-in storm capture

In figure 6.4, images of TARA between the time interval of 13:25-13:46 UTC are presented. The left images are the original TARA images, which were taken at a 45 degrees angle scan. This angle is the main reason for the tilted shapes which can be observed in all images on the left of the figure. The right images represent the same TARA data however corrected for this 45 degrees angle. The images are generated simply to ease the 45 degree angle implementation for the reader. Note here that these images are just a first approximation for the 45 degrees angle correction because due to very chaotic and non-homogeneous wind situations at the time of the case, also a correction for the particle path induced by wind has to be executed. However, this particle path correction is outside of the scope of this research.

When inspecting the reflectivity image in figure 6.4, on the most left side of the heavy precipitation cell (indicated with a 45 dBZ contour) the bounded weak echo can be found. This conclusion is not solely based on the reflectivity results. When inspecting the vertical Doppler velocity image, large updrafts are found around where the BWER is indicated to be.

From the horizontal wind speed, the 3rd image from the top, high wind shear signatures are found at low altitude, near the ground and at high altitude, again around the 45 dBZ reflectivity contour. The time of the observed most significant wind shears, around (13:40 UTC) is in agreement with wind speed and direction observations from the tower mast, which will be addressed in the following section (section 6.3). From the horizontal wind direction image, the bottom image in figure 6.4, again a region of wind shear can be found around the 45 dBZ contour. In the most extreme case the wind is coming from approximately 280 degrees (indicated in red/yellow) and flows over in wind directions from around 100 degrees (indicated in blue). This area is exactly a 180 degrees difference in wind direction, a feature which indicates rotation. Furthermore, the dark blue pixels within the storm may look interesting but they are just measurements from wind coming from the North, which means that they are on the edge of 360 (dark red) and 0 (dark blue) degrees, thus in fact the same direction.

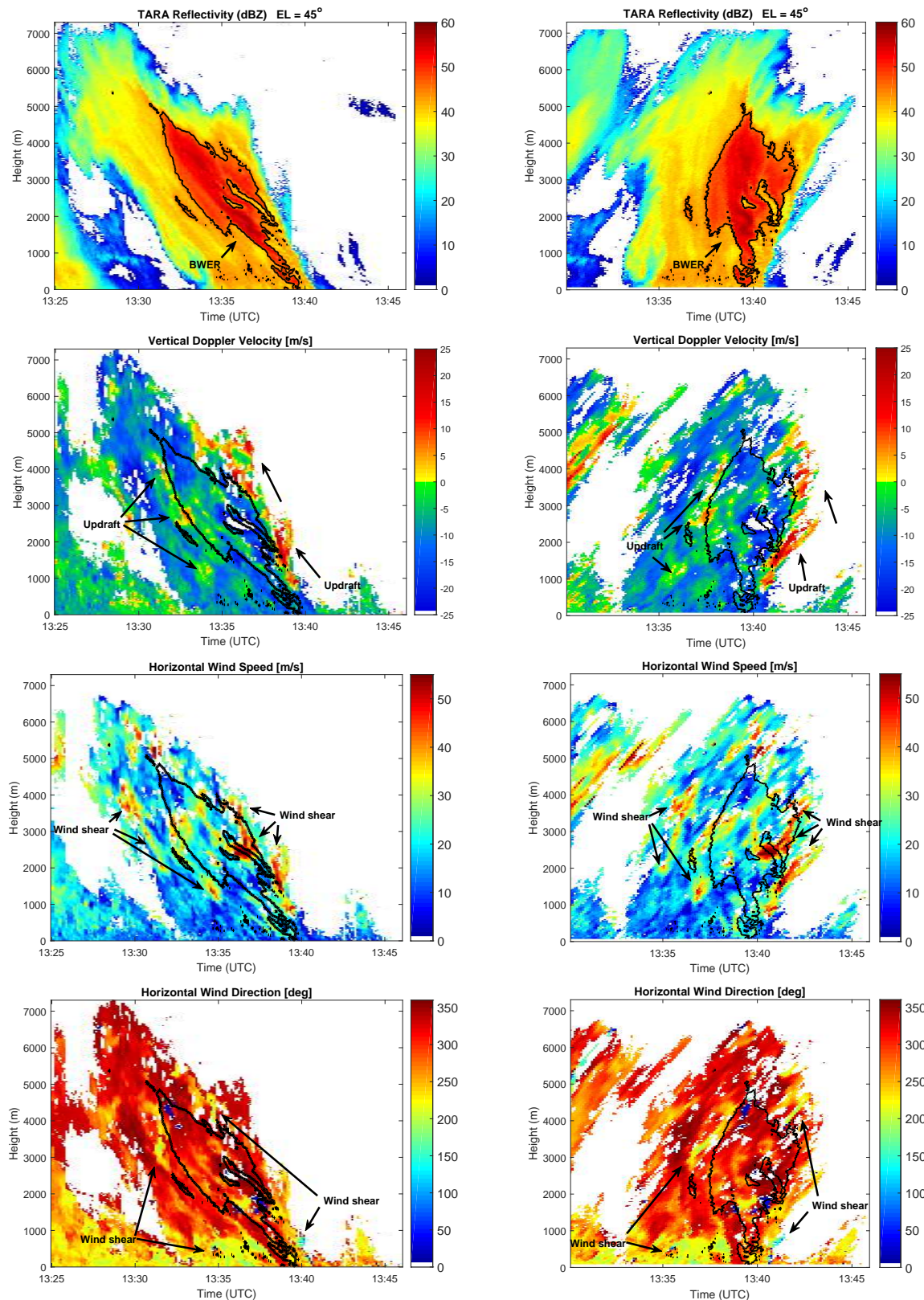


Figure 6.4: From top-down: TARA reflectivity, the bounded weak echo region can be found on the left side of the reflectivity contour. In the second panel, the vertical Doppler velocity, strong updrafts are observed around the location of the weak echo region. Significant wind shear in the horizontal wind speed panel is present around the weak echo region of the cell. From the bottom panel horizontal wind direction is presented with again wind shear in the lower region of the cell indicating rotation. In all images a contour line in black representing 45 dBZ reflectivity is depicted.

6.3 CESAR in-situ tower measurements

In figure 6.5 wind speed and wind direction profiles from the CESAR in-situ tower measurement dataset between a time interval of 12:00-15:30 UTC are presented. When inspecting the wind speed it can be observed that until 13:00 UTC the wind speed remains very uniform, then starting at 13:00 UTC it suddenly shows a drop. The largest drop in wind speed is found between 13:30 and 13:40 UTC. In the previous section, results from TARA indicated that a storm cell passed CESAR between 13:35-13:40 UTC and therefore this drop is associated with wind shear due to the passing of a rotating storm cell. Note that during the measurement interval wind direction remains quite uniform. This is mainly due to the fact that an average wind direction over the time interval of 10 minutes is taken. Thus, even in the event of major turbulence where the wind direction varies greatly, no significant differences in wind direction data may be found in due to the averaging of the data over time.

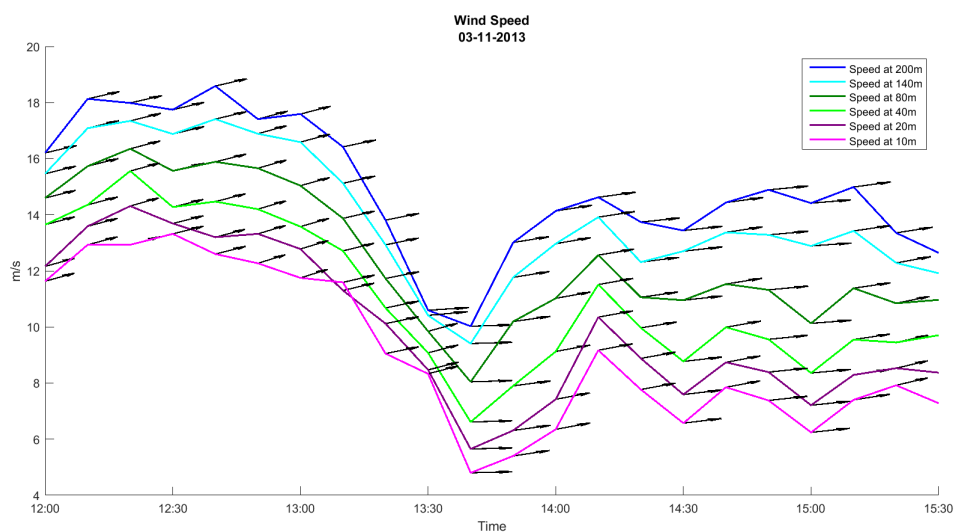


Figure 6.5: Wind speed and direction observed at the CESAR tower at height ranging from 10 to 200 meter, between 12:00 - 15:30 UTC. Between 13:30-13:40 UTC a significant drop in wind speed can be observed which is identified as wind shear due to the passing of a rotating storm cell.

6.4 35GHz CloudRadar

Due to the fact that the CloudRadar operates at 35 GHz, it is strongly sensitive to small hydrometeors and signal attenuation in case of moderate to heavy rain.

When inspecting figure 6.6, no signal can be observed at a height between 3000 and 1000 meters and between the time interval 13:30-13:35 UTC. This is not due to signal attenuation, as no data would be available along the radial with height, which is the case here. Therefore, this area can be indicated as a bounded weak echo region.

From TARA observations it can be confirmed that this bounded weak echo region is the same BWER as observed with TARA which is presented in figure 6.4. The 5 minutes time difference between the signatures can be explained due to the fact that with its 45 degrees TARA is basically looking into what is coming. This complementary observation, strongly supports the theory that it is a rotating cell which is passing Cabauw.

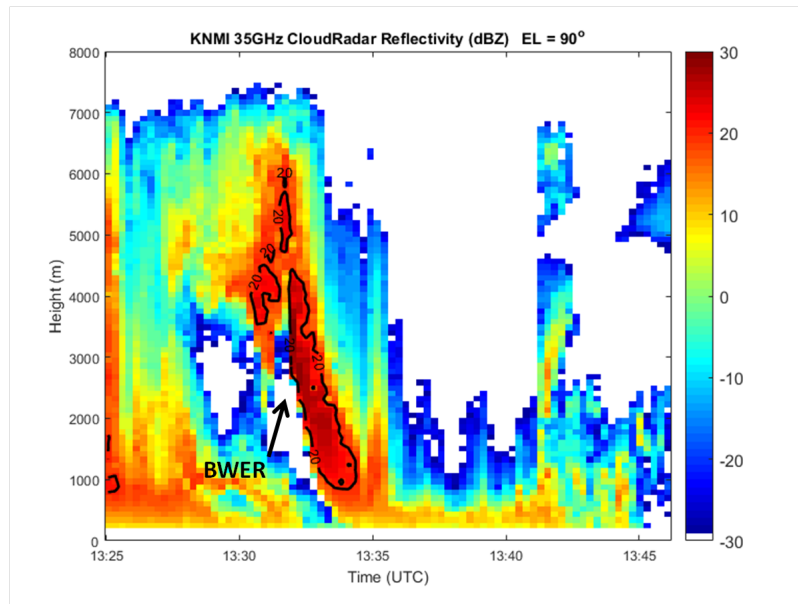


Figure 6.6: Measurements of KNMI’s 35GHz CloudRadar situated at CESAR observatory. The bounded weak echo region is clearly visible between time interval 13:30-13:35 UTC.

6.5 Wind profiler

As last verification measurement system, the KNMI’s wind profiler is used, which takes an average wind profile per range bin with a resolution of 30 minutes. This temporal resolution is too low to enable the profiler to distinctively recognize tornadic signatures of a small rotating cell, as the cell moves fast and is even less than 5 minutes present within the field of view of the profiler. The result of this low temporal resolution is that the profiler’s observations are very smoothed out and too uncertain to make any specific comments on the plot presented in figure 6.7. However it may be noted, that in the time interval of 13:15-13:45, the interval during which the cell passes, there is a significant difference in wind speed and wind direction in comparison with its preceding and subsequent observation; it is clear that there was an increase in turbulence during that time interval.

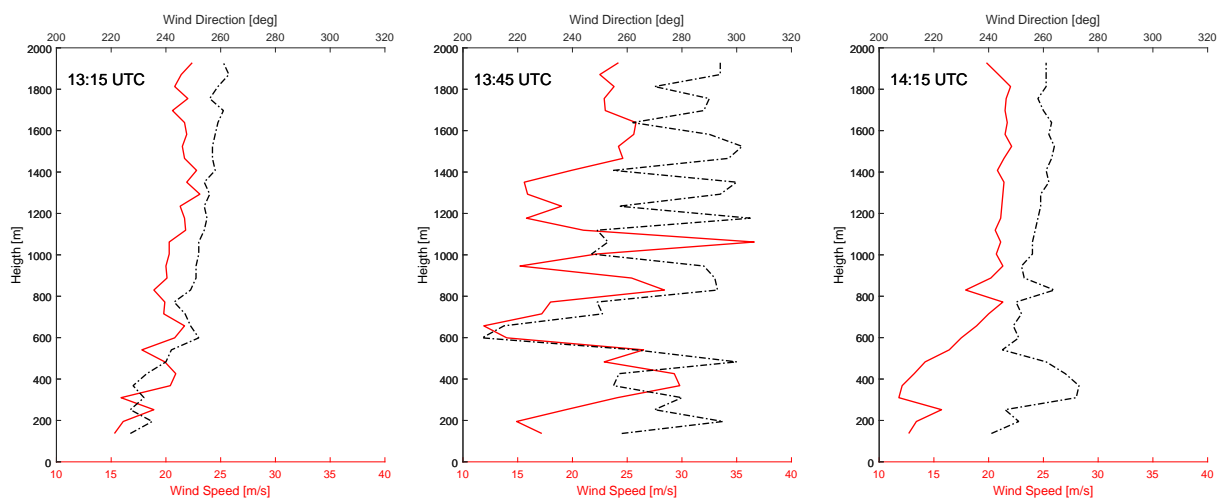


Figure 6.7: Measurements of KNMI's Wind Profiler situated at CESAR observatory. The red line represents wind speed in m/s, the black dotted line is wind direction, both as function of height. The image interval starting times are 13:15, 13:45 and 14:15 UTC, respectively. The observations at 13:45 UTC show a significant large difference of both parameters as a function of height with respect to the 13:15 and 14:15 UTC observations.

Conclusions

In this chapter first the main research question stated at the introduction will be answered, this is followed by the subquestions.

Can the high resolution X-band radar IDRA detect a typical small scale tornado?

Yes, IDRA is very well capable of detecting small scale tornadoes. Two main key drivers can be appointed for this positive outcome:

- high resolution features of the radar
- Doppler radial velocity and spectrum width outputs

The high spatial and temporal resolution of IDRA plays a big role in the detection of the tornadic signature wind shear, due to the small scale of the event. IDRA was able to observe a wind shear cell with the size of approximately 700x700 meter which proved to be the rotating cell which produced a tornado 20 minutes later which had its touchdown at Wijk bij Duurstede. Such an observation are not producible by KNMI weather radar because of its large spatial resolution.

The Doppler radial velocity and spectrum width proved to be the driving outputs of IDRA in order to detect significant tornadic signatures. IDRA proved to be able to make a good distinction between significant potential hazardous wind shear and more homogeneous wind situations.

Now that it has been made clear that the answer to the main research question has a positive outcome, the subquestions can be answered:

1. What are the most significant detection signatures found by IDRA?

IDRA clearly showed to be very sensitive to gate to gate wind shear induced by the rotating cell. It can be concluded that with just 2 output parameters, IDRA is already able to detect tornadic signatures. These parameters are: radial Doppler velocity in order to find high wind shear pixels and the spectrum width in order to verify whether the high wind shear is not erroneous or unreliable. Next to wind shear, the IDRA observed the famous hook echo and v-notch with its reflectivity scans. The specific differential phase parameter showed some interesting signatures as well, but due to missing radial data and unreliable polarimetric parameters this could not be verified.

2. What are the tornado signatures observed by additional verifying measurement systems?

From the KNMI near real-time C-band radar's reflectivity images, both the hook echo and the v-notch signature were well observed. No significant wind shear signatures were present, thus no exact location of the tornado itself could be established from this radar. From TARA data the bounded weak echo region including wind shear signatures can be found. The tower wind measurements show a large drop in wind speed which is associated with the rotating cell passing and the 35 GHz Cloudradar displayed the same bounded weak echo region as found with TARA. Unfortunately on none of the additional verifying measurement systems other tornadic signatures such as debris, wind shear or high spectrum width could be found.

Discussion & Recommendations

In this chapter a discussion on the research question is opened and further recommendations are given in order to improve tornado detection and warning abilities in the Netherlands.

More research on and monitoring of tornadoes in Europe As indicated in the introduction, not much information is available on tornadoes and what the impact of climate change can mean to its frequency and intensity in Europe. Therefore it is recommended to monitor the outbreak of these events better and to conduct more research on the frequencies, locations and intensity of tornadoes in Europe, over the past years. Both data should be used in order to construct a scenario for the future.

Importance of early warning signals and its implementation IDRA has proven to be able to detect areas of high wind shear that indicate the location and the direction to which the rotating cell develops. The fact that this information was available at least 20 minutes prior touch down is very valuable.

One of the main reasons that there were no injuries or fatalities reports as result of the tornado event on the 3rd of November 2013 is partly because the touchdown was on a Sunday afternoon at an industrial area. Little to no human activity can be found in such areas on such particular days. Though, such 'fortunate' circumstances might not always arise and in cases where risk arises a 15 minute warning time is crucial and may save lives.

It is therefore recommended to look further into what role a high resolution radar such as IDRA can contribute as an early warning signal detector. During such research, focus should be put on implementation of IDRA signals such as described in this report to already existing weather warning systems. One could think of designing an algorithm based on Doppler velocity gradient detection, that gives out a warning to for instance the KNMI when larger gradients are detected verified with a large spectrum width at the large gradient locations. Subsequently, this warning can then be verified and specific regions in the Netherlands can be alarmed for potential tornadic hazards.

In order for high resolution radars to become part of a early warning signal systems, a significant areal coverage should be available. As IDRA is next to the newly implement X-band radar in Rotterdam one of the only two high resolution radars in The Netherlands, the network is too sparse and should be first expanded. It should be mentioned that motivation for such expansion does not exclusively have to be hazardous weather detection, as it obviously brings many other interesting objectives with it, such as pollution and insect and bird migration monitoring.

Conduct further research with use of polarimetric radars It is clear that IDRA is sensitive enough to observe small scale rotation cells that might develop tornadoes. In this case study all polarimetric radar outputs of IDRA obtained were flagged as unreliable and therefore not analyzed. It is recommended to perform more research on high resolution polarimetric characteristics of small scale rotation cells. Special attention should be paid to the specific differential phase as it showed encouraging signals in this case.

In the case that high resolution polarimetric signatures are very clearly distinguishable as well, the earlier suggested algorithm for early signal detection can then be enforced and made more reliable.

When conducting this suggested research, it is recommended to make sure that IDRA data set is fully available; it should show the full radar PPI without missing radial and has to have a continuous data set over time with reliable polarimetric outputs.

Bibliography

- Knmi datacentrum - waarnemingen & rekenmodellen.* <https://data.knmi.nl/portal/KNMI-DataCentre.html>.
- Aydin, K., T. A. Seliga, & Balaji, V. 1986. Remote sensing of hail with a dual-linear polarization radar. *Journal of applied meteorology*, **25**, 1475–1484.
- Battan, L.J. 1973. Radar observation of the atmosphere. *The university of chicago press*.
- Beard, K.V., & Chuang, C. 1987. A new model for the equilibrium shape of raindrops. *Journal of the atmospheric sciences*, **44**, 1509–1524.
- Berne, A., Delrieu G. Creutin J.-D. Obled C. 2004. Temporal and spatial resolution of rainfall measurements required for urban hydrology. *Journal of hydrology*, 166–179.
- Bluestein, H.B., & Unruh, W.P. 1989. Observations of the wind field in tornadoes, funnel clouds, and wall clouds with a portable doppler radar. *Bulletin of the american meteorological society*, **70**, 1514–1525.
- Bluestein, H.B., Ladue J.G Stein H., & Speheger, D. 1993. Doppler radar wind spectra of supercell tornadoes. *Monthly weather review*, **121**(8), 2200–2222.
- Brooks, E. B., G. W. Carbin-P.T. Marsh. 2014. Increased variability of tornado occurrence in the united states. *Science*, **346**(6207), 349–352.
- Chuang, C.C., K.V. Beard. 1990. A numerical model for the equilibrium shape of electrified raindrops. *Journal of the atmospheric sciences*, **47**(11), 1374–1389.
- Collier, C.G. 2009. On the propagation of uncertainty in weather radar estimates of rainfall through hydrological models. *Meteorological applications*, 35–40.
- Diffenbaugh, N. S., Scherer M. & Trapp R. J. 2013. Robust increases in severe thunderstorm environments in response to greenhouse forcing. *Proceedings of the national academy of sciences*, **110**(41), 16361–16366.
- Doviak, R.J., & Zrnicek, D.S. 2006. *Doppler radar and weather observations*. Dover Publications.
- Fabry, F., Bellon A. Duncan M. R. & Austin G. L. 1994. High resolution rainfall measurements by radar for very small basins: the sampling problem reexamined. *Journal of hydrology*, **161**, 415–428.
- Fang, M. 2004. Spectrum width measured by wsr-88d: Error sources and statistics of various weather phenomena. *Journal of atmospheric and oceanic technology*, **21**(6), 888–904.

- Figueras I Ventura, J. 2009 (November). *Design of a high resolution x-band doppler polarimetric weather radar*. M.Phil. thesis, Delft University of Technology.
- Giangrande, S. E., & Ryzhkov, A. V. 2005. Calibration of dual-polarization radar in the presence of partial beam blockage. *Journal of atmospheric and oceanic technology*, **22**(8), 1156–1166.
- Gorgucci, E., G. Scarchilli V. Chandrasekar. 1999. Specific differential phase estimation in the presence of nonuniform rainfall medium along the path. *Journal of atmospheric and oceanic technology*, **16**(11), 1690–1697.
- Heijnen, S.H., Ligthart L.P. Russchenberg H.J.W. 2000. First measurements with tara: An s-band transportable atmospheric radar. *Physics and chemistry of the earth, part b: Hydrology, oceans and atmosphere*, **25**, 995–998.
- Iguchi, T., R. Meneghini H. Kumagai. 1992. Radar depolarization signatures of rain in cumulus clouds measured with a dual-frequency air-borne radar. *In: Igarss '92; proceedings of the 12th annual international geoscience and remote sensing symposium, houston, tx*.
- KNMI. 2013. <https://www.knmi.nl/over-het-knmi/nieuws/windhoos-in-wijk-bij-duurstede>.
- KNMI. 2014. *Uitleg over windhozen*. <https://www.knmi.nl/kennis-en-datacentrum/uitleg/windhozen>.
- Kumjian, M.R., & Ryzhkov, A.V. 2008. Polarimetric signatures in supercell thunderstorms. *Journal of applied meteorology and climatology*, **47**, 1940–1961.
- Ladue, J.G., & Mahoney, E. 2006. Implementing the new enhanced fujita scale within the nws. *In: Preprints*. American Meteorological Society, St. Louis, MO.
- Leck, R.P. 2009. Use of radio spectrum for use of radio spectrum for meteorology: Weather, water and climate monitoring and meteorology: Weather, water and climate monitoring and prediction prediction. *In: Itu/wmo seminar, session 6*.
- Leijnse, H., Uijlenhoet R. van de Beek C.Z. Overeen A. Otto T. Unal C.M.H. Dufournet Y. Russchenberg H.W.J. Figueras I Ventura J. Klein Baltink H. Holleman I. 2010. Precipitation measurement at cesar, the netherlands. *Journal of hydrometeorology*.
- Leon, L. 2015. *Inel5607 introduction to radar meteorology, lecture slides by university of puerto rico*.
- Liguori, S., Rico-Ramirez M.A. Schellart A.N.A. Saul A.J. 2012. Using probabilistic radar rainfall nowcasts and nwp forecasts for flow prediction in urban catchments. *Atmospheric research*, **103**, 80–95.
- Lopez, R. E., & Aubagnac, J. P. 1997. The lightning activity of a hailstorm as a function of changes in its microphysical characteristics inferred from polarimetric radar observations. *Journal of geophysical research*, **102**, 16799–16813.
- M., Beljaars A. C., & Bosveld, F. C. 1997. Cabauw data for the validation of land surface parametrization schemes. *Journal of climate*, **10**, 1172–1193.
- Marshall, J. S. & Palmer, W. M. K. 1948. The distribution of raindrops with size. *Journal of meteorology*, **5**(4), 165–166.
- Moore, T.R., Damon Matthews H. Simmons C., & Leduc, M. 2015. Quantifying changes in extreme weather events in response to warmer global temperature. *Atmosphere-ocean*, **53**(4), 412–425.

- NOAA. 2014. <http://www.srh.noaa.gov/abq/?n=preptornadoes>.
- NOS. 2013a. http://nos.nl/artikel/574533-schade-windhoos-zeker-eeen-miljoen.html?utm_source=feedburner&utm_medium=feed&utm_campaign=Feed%3A+nosnieuwsbinnenland+%28NOS+Nieuws+-+Binnenland%29.
- NOS. 2013b. <http://nos.nl/video/570123-binnenlands-weerbericht-2-november-2013.html>.
- Ochoa-Rodriguez, S. 2014. *Impact of spatial and temporal resolution of rainfall inputs on urban hydrodynamic modelling output: A multi-catchment investigation*. Internal publication. Imperial College London.
- Otto, T., H.W.J. Russchenberg. 2011. Estimation of specific differential phase and differential backscatter phase from polarimetric weather radar measurements. *Ieee, geoscience and remote sensing letters*, **8**(5), 988–992.
- Otto, T. 2013. *A short course on radar meteorology*. <http://collegerama.tudelft.nl/mediasite/SilverlightPlayer/Default.aspx?peid=1805993fac954c3fba5855bce7e6a86e1d>.
- Paquin, D., de Ela R. & Frigon A. 2014. Change in north american atmospheric conditions associated with deep convection and severe weather using crcm4 climate projections. *Atmosphere-ocean*, **52**(3), 175–190.
- Probert-Jones, J. R. 1962. The radar equation in meteorology. *Quarterly journal of the royal meteorological society*, **88**(378), 485–495.
- Reinoso-Rondinel, R., C. Unal H. Russchenberg T. IJpelaar Y. Dufournet. 2014. Polarimetric weather signatures and doppler spectral analysis of a convective squall line. *The eighth european conference on radar in meteorology and hydrology*.
- Ryzhkov, A.V., Zrnice D.S Schuur T.J. Burgess D.W. 2005. Polarimetric tornado detection. *Journal of applied meteorology*, **44**, 557–570.
- Sachidananda, M., D. Zrnice. 1986. Differential propagation phase shift and rainfall rate estimation. *Radio science*, **21**(2), 235–247.
- Sachidananda, M., & Zrnice, D. S. 1986. Differential propagation phase shift and rainfall rate estimation. *Radio science*, **21**(2), 235–247.
- Straka, J.M., & Zrnice, D. S. 1993. An algorithm to deduce hydrometeor types and contents from multiparameter radar data. *Pages 513–515 of: Society, American Meteorological (ed), 26th international conference on radar meteorology*.
- Tanamachi, R. L., Bluestein H. B. Houser J. B. Frasier S. J., & Hardwick, K. M. 2012. Mobile, x-band, polarimetric doppler radar observations of the 4 may 2007 greensburg, kansas tornadic supercell. *Monthly weather review*, **140**, 2103–2125.
- Uijlenhoet, Remko. 2001. Raindrop size distributions and radar reflectivityrain rate relationships for radar hydrology. *Hydrology and earth system sciences*, **5**(4), 615–627.
- Unal, C. 2014. *Delft university of technology: Atmospheric observation, radar meteorology, lecture 1*. Internal Publication.
- Unal, C. M. H. 2009. Spectral polarimetric radar clutter suppression to enhance atmospheric echoes. *Journal of atmospheric and oceanic technology*, **26**, 833–845.

- Van Den Broeke, M.S., Jauernic S.T. 2014. Spatial and temporal characteristics of polarimetric tornadic debris signatures. *Papers in the earth and atmospheric sciences*, **53**, 2217–2231.
- van der Kolk, Thomas. 2013 (November). *Weerplaza: Nederland werd getroffen door twee tornado's*. Trouw.
- van Nederland, Hart. 2013. <http://www.hartvannederland.nl/nederland/utrecht/2013/windhoos-wijk-bij-duurstede-was-tornado/>.
- Vivekanandan, J., V. N. Bringi, & Raghavan, R. 1990. Multiparameter radar modeling and observations of melting ice. *Journal of atmospheric science*, **47**, 549–564.
- Wang, Y., V. Chandrasekar. 2009. Algorithm for estimation of the specific differential phase. *Journal of atmospheric and oceanic technology*, **26**(12), 2565–2578.
- Wurman, J., Gill S. 2000. Finescale radar observations of the dimmitt, texas (2 june 1995), tornado. *Monthly weather review*, **128**, 2135–2164.
- Zrnic, D. S., & Istok, M. 1980. Wind speeds in two tornadic storms and a tornado, deduced from doppler spectra. *Journal of applied meteorology*, **19**(1405-1415).
- Zrnic, D. S., N. Balakrishnan C. L. Ziegler V. N. Bringi K. Aydin, & Matejka, T. 1993. Polarimetric signatures in the stratiform region of a mesoscale convective system. *Journal of applied meteorology*, **32**, 678–693.
- Zrnic, D. S., R. J. Doviak, & Burgess, D. W. 1977. Probing tornadoes with a pulse doppler radar. *Quarterly journal of radar meteorology society*, **103**(438), 707–720.
- Zwart, Baltus. 1994. De anatomie van de windhoos. *Meteorologica*, **94**(1).